



# Fluid-structure interaction of thin flexible bodies in multi-material multi-phase systems

Mehdi Vahab, Mark Sussman, Kourosh Shoele\*

Florida State University, Tallahassee, FL 32306, United States of America

## ARTICLE INFO

### Article history:

Received 12 December 2019

Received in revised form 21 October 2020

Accepted 13 November 2020

Available online 19 November 2020

### Keywords:

Fluid-structure interaction

Multi-phase flow

Phase-change

Boiling process

Thin structure

## ABSTRACT

A numerical approach for the modeling and simulation of fluid-structure interaction (FSI) in multi-material and multi-phase systems with potential phase-changes dynamics is presented. The boundary conditions at the interface between the fluids and structures are enforced using an immersed boundary technique to couple the Eulerian multi-material solver to the Lagrangian structural solver and maintain the solution algorithm's efficiency. The phase-change dynamics are modeled to consider the volume expansion/shrinkage due to the density difference in materials. The algorithm for material phase-change includes a sub-grid model near triple points and benefits from the volume-conservative continuous moment-of-fluid (CMOF) reconstruction method for smooth material domain representation. A systematic stability criterion for the coupled problems with the proposed FSI technique is derived, and the accuracy of the method is verified and tested with multiple canonical problems. The technique is employed to explore the effects of the active vortex generation of a flapping plate on the momentum and thermal dynamics of the nucleate pool boiling phenomenon in a cross-flow in two and three-dimensional setups.

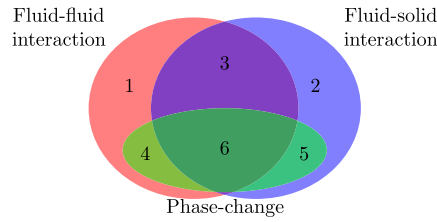
© 2020 Elsevier Inc. All rights reserved.

## 1. Introduction

The analytical and numerical modeling of multi-material and multi-phase systems, including fluid-fluid or fluid-structure interaction and phase-change, are intricate due to the multiplicity of involved materials/phases and physical phenomena. The multi-material systems that involve at least one of these properties are prevalent across many sciences and engineering disciplines (see Fig. 1 & Table 1 for some examples). Despite quite a few previous works on the modeling and simulation of each phenomenon individually, few techniques are put forward to simulate the fluid-structure interaction in the presence of several materials and mass transfer between different phases in a general approach. In the meantime, to investigate the physics of systems that involve many of these properties, such as thermal management systems, a coupled, efficient, and accurate computational modeling approach is required. For example, high flux thermal management systems using two-phase heat transfer methods with intricate surface geometries and actuation have been explored for miniature computer processors and power electronics with large power consumption and thermal loads as well as for electric cars, boats, and airplanes. The thermal design of these systems requires better modeling of the multi-phase processes in complex dynamic geometries. Another example is the design of passive and semi-active heat pipe systems, wherein better numerical modeling is needed to understand the working conditions of the system and the role of multiscale material interaction, heat transfer, and phase-change dynamics [1,2]. Similarly, thermal management of the cryogenic applications using novel approaches

\* Corresponding author.

E-mail address: kshoele@fsu.edu (K. Shoele).



Examples	Phenomena
1 Bubbly flow, droplet interaction	Surface tension
2 Particle-laden flow, droplet-surface interaction	Momentum and energy transfer
3 Two-phase flow in porous media	Surface tension & momentum and energy transfer
4 Two-phase heat exchangers	Boiling and condensation
5 Aircraft icing	Solidification and melting
6 Cavitation	All of the above

**Fig. 1 & Table 1.** List of dynamic processes in the presence of multi-material systems with possibility of phase change and sample applications which are governed by them.

is another emerging application in which a better understanding of cryogenic fluids and multi-phase dynamics during their storage and transportation are essential for long-range space exploration [3,4]. We propose a numerical method for the multi-material system with fluid-structure interaction and phase-change dynamics, implemented for the thin, flexible bodies, and explain how the proposed approach permits a unified and efficient computational method for studying these phenomena.

### 1.1. Multi-material systems

Various computational methods have been suggested for the simulation of multi-material systems with the fronts/interfaces such as material interfaces and shocks [5,6]. One approach is to define the interfaces explicitly using marker points. These marker points may influence the fluid grid generation (moving material meshes) or be independent of fluid grids [7]. The Lagrangian methods with moving meshes are ideal when the interface is static or has small deformation to avoid the computational cost of remeshing procedures and mesh entanglement problems. Another approach is to define one identifying function or a combination of functions that can be used to identify the material domains. The most common techniques in this category are level set (LS) [8], volume-of-fluid (VOF) [9], moment-of-fluid (MOF) [10] methods. The interface may be derived directly from these functions (e.g., zero-level in the level set method), or reconstructed from the information these functions contain. Usually, these reconstructions are not unique and dependent on the employed material domain functions and the effect of non-local data on the computational cell. For example, VOF is used for the interface reconstruction in the following methods: simple line interface calculation (SLIC) [11], piecewise linear interface calculation (PLIC) methods [12–15], and least-squares volume-of-fluid interface reconstruction algorithm (LVIRA) [16,17]. More recently, the moment-of-fluid (MOF) method has been introduced to use the centroid of a material domain in a computational cell along with the volume of the fluid data to create a unique representation of the interface using the local data near each computational cell. Another major challenge of multi-material techniques is related to the situation in which more than two materials are present ( $N > 2$ ) where specialized techniques are needed to generalize two-material reconstruction methods to multi-material scenarios. Examples are independent dissections, onion-skin model (parallel dissections), nested dissection, and serial dissection (see [18] for more details). However, the reconstruction results from these methods are dependent on the material order, which in principle could result in nonidentical reconstruction for the different ordering of materials. One antidote is to use power diagram (PD) technique [19,20]. Alternatively, the MOF reconstruction methods such as MOF-SD and MOF-BTD [18] also provide an automatic ordering solution to have a unique second-order reconstruction of the interface in multi-material cells. Also, if a specific material ordering is available, e.g., contact angle on a surface, a specific algorithm can be developed to reconstruct multimaterial cell imposing certain constraints [21].

### 1.2. Fluid-solid interaction

The presence of interacting fluid and solid materials with comparable dynamic timescales necessitates specific models to capture fluid-solid interactions (FSI) correctly. These models are even more vital if the solid structure undergoes large deformation. The FSI modeling techniques may be categorized by the computational grids, solver interconnections, and degree of coupling of respective fluid and structure domains. Here we give a short description of these properties, and some example works, however, more detailed review of these methods and their characteristics can be found in [22,23].

Generally, it is more convenient to study solid materials in a coordinate system attached to the structure. Therefore, many of FSI methods use a computational grid that conforms to the solid geometries and track the fluid-solid interface. Other methods only employ a static grid, and generally, a moving structure does not coincide with the computational grid.

In particular, if the structure is flexible and undergoes large deformation, the non-conforming grids are preferred, since the structural deformation may result in a distorted or entangled fluid mesh for conforming grids. They also require frequent computationally expensive remeshing, which affects the overall accuracy of the methods. Another aspect of the FSI methods is the coupling of the mathematical formulation and numerical solution for fluid and solid sub-domains. The monolithic methods try to use the same formulations for fluid and solid materials with implicit fluid-structure relation. This approach usually leads to a unique set of equations to describe the whole system altogether, which may become complex by including further interfacial dynamics. In contrast, the partitioned methods model the fluid and solid materials separately, and impose boundary condition or do state variable transfer at the material interfaces. The numerical methods developed for single-phase fluid or solid materials may be applied to partitioned FSI methods with less modification, requiring less effort and time for code development.

A successful family of FSI techniques that use the partitioning approach is the immersed boundary methods (IBM) introduced by Peskin [24,25]. This approach couples the Eulerian framework of the fluid and the Lagrangian description of the solid using the integral transformation with Dirac delta kernel function and forms a mathematically consistent framework to represent the fluid-structure interaction effect in the governing equation of the fluid. While some methods are designed in the continuous formulation level and use the continuous forcing approach to include the forcing term in the continuous form of the fluid momentum equation (independent of the discretization method) [26,27], others directly target the discretized fluid equations by considering a sharp boundary condition at the fluid-structure interface [28–30]. The forcing term can be calculated from the structural mechanics and the strain energy function of the solid material. Alternatively, the forcing term can be designed to impose a no-slip boundary condition with a projection-based [31] or feedback frameworks [32–35]. These methods essentially perform a Dirichlet-to-Neumann boundary condition transformation at the fluid-solid interfaces. Compared to the original immersed boundary method, they lead to the less spurious oscillation at in fluid-structure interface for flexible structures that have different densities than the surrounding fluids [36,37]. More information about FSI methods can be found in [38,39]

### 1.3. Phase-change dynamics

The phase-change dynamics at the interface between adjacent materials can be described using models with different degrees of complexity. A common technique for two-phase systems of single material is to use the enthalpy to model phase-change and determine phase domains at the same time [40–42]. This method by itself does not require explicit treatment of the moving boundaries, and it has been abundantly employed to model single material phase-change (commonly solidification process) [43,44], or is used along with interface tracking methods [45–48]. The application of the enthalpy formulation is suitable for systems with weak energy jumps such as solidification of metals [47]. A more general approach is to use the energy jump condition at the phase-change interface and directly relate it to the rate of phase-change mass transfer [49]. Although this method does not account for the kinetic energy contribution [50], it has been used extensively since it does not require empirical coefficients [51]. The Schrage model [52], based on the kinetic theory of gases, is another phase-change model that has been used frequently for boiling/condensation systems [53–55]. This technique uses empirical accommodation coefficients for different flow and phase-change systems [56,57], which makes it less practical for a general-purpose approach. Similarly, the model proposed by Lee [58], which correlates the difference of the interface and saturation temperatures to the rate of phase-change, also needs an empirical coefficient, which has to be determined by comparison to experiments in a case-by-case scenario. The modeling of fluid evaporation would also need specific treatments that are different from the boiling process. See the work by Villegas et al. [59] for a method that allows the treatment of both evaporation and boiling.

Other than the macro-models mentioned above, there have been efforts to simulate the intricate thermal and interfacial dynamics explicitly in multi-material regions. These approaches target the phase-change at the triple point regions, e.g., where the liquid, vapor, and a hot surface come into contact, using a micro-region [60,61] or micro-layer [62,63] to account for the enhanced phase-change due to large temperature gradients in those sites. These methods are effective since they are independent of spatial discretization at the triple point [64].

### 1.4. Multi-physics modeling and simulation

The primary physical phase-change process in the aforementioned problems contains at least two phases, the source, and target phases, and therefore most of the numerical methods for **multi**-material systems with phase-change dynamics are inherently designed to consider only two phases [51,53,55,62,65,66]. Although this consideration is sufficient to study the phase-change process, it lacks the generality needed to investigate a wide range of problems with more than two materials. On the other hand, the phase-change dynamics of multi-material systems can be very complex and pose significant challenges to numerical methods for multi-material problems [15,67–72]. Very few techniques can capture phase-change dynamics in the presence of more than two materials. Vu et al. [73] extended the two-phase front-tracking/finite difference

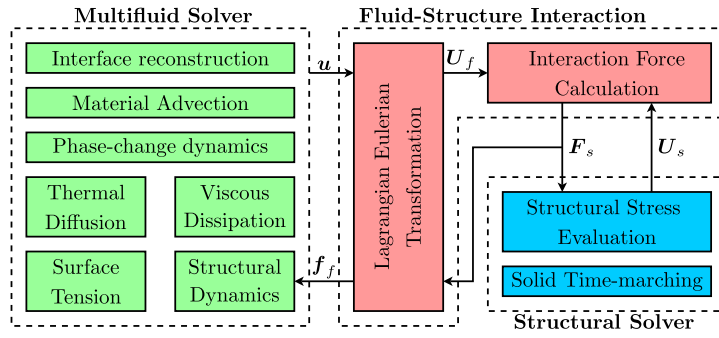


Fig. 2. Partitioning and interaction of the fluid and solid solvers and the FSI methodology.

methods by Esmaeeli and Tryggvason [65,74] to model the solidification of a liquid drop on a substrate in a tri-material configuration. Vahab et al. [75] used a coupled level-set and moment-of-fluid method to simulate the solidification process in a multi-material formulation.

Moreover, most of the proposed numerical methods are designed on the static mesh assumption and Eulerian description of the fluids, which prevents them from being used for applications with large boundary motion and deforming structures. In particular, it is very challenging to simulate very thin structures (e.g., fibers, beams and shells) in the Eulerian flow simulations when the thickness of the structure is much smaller than other dimensions of the structure. For modeling thin structures efficiently, one can take advantage of the affine transformation through the thickness and relate the motion of any point in the structure to the motion of the center-line for the fiber case or the mid-surface for the shell structure. The procedure reduces the dimension of the structural dynamics equations by one (for shell or two-dimensional beam structures) or two (for three-dimensional fibers/beams). The Lagrangian methods are favorable for solving the structural dynamics of these geometries in the coordinate system attached to the structures. To model FSI, a mechanism is required for transferring the interacting quantities (such as force and velocity) between structure and fluid in their corresponding Eulerian and Lagrangian forms. The immersed boundary (IB) method [24] and its variants [27,32,33,35,76] are well-established approaches to include structures with arbitrary geometries within the Cartesian-grid fluid solvers. Only very recently, the technique has been extended to two-phase flows by Wang et al. [77]. Other approaches have also been used to study fluid-structure interaction in multi-phase flow systems. Among all, Wang et al. [78] combined a Eulerian finite volume multi-phase solver with a Lagrangian finite element structure solver using a two-phase exact Riemann solver in embedded boundary computational framework. Yang et al. [79] used a one-fluid formulation of two-phase flow and applied immersed elastic energy function for FSI. However, these techniques are mostly applicable for solid phases with large volumes, and their extension to thin structures often results in a much smaller time step or substantially increase number of required iterations to capture dynamics at the fluid-solid interfaces.

### 1.5. The proposed computational method

Here we adopt the immersed boundary method using the force feedback penalty coupling initially proposed by Goldstein et al. [32] to include thin structural bodies in multi-phase flow fields. This approach is later extended to include flexible structures while accounting for the solid mass [36] and successfully used for the study of flapping flexible fins [80], hovering using flexible wings [81], the flow-induced fluttering of a flexible reed and its effect on convective heat transfer [82], and heat transfer enhancement by flexible flags in a Poiseuille channel flow [83].

We present a computational approach for the numerical modeling and simulation of systems that include multiple fluids (more than two) and thin deformable structures. The fluids are incompressible, immiscible, and may undergo phase-change. This method is developed to study FSI in multi-material systems that surface tension, heat transfer, and phase-change are the significant dynamics (see Fig. 2). To the best of our knowledge, this is the first effort to extend such an FSI approach to multi-material/multi-phase systems. The problem description and mathematical formulation of the problem are presented next two sections. In the fourth section, we discuss the numerical methods employed here. The computational tests are presented in the fifth section, which includes canonical tests to evaluate the performance and accuracy of the combined computational method, a heuristic FSI stability criteria, and an application of the proposed algorithm. The final section includes the summary and conclusion of this study and suggested future works.

## 2. Problem description

The problem domain can contain multiple fluids, bulk solids, and thin structures. Here are the restrictions that are assumed for the problem set up.

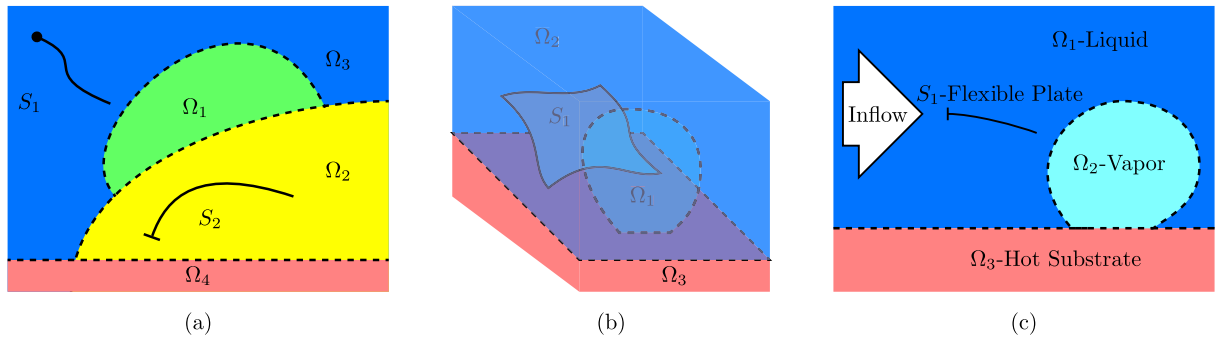


**Fig. 3.** Schematic view of general problem setup in a) 2D flow and 1D (fiber) structures and b) 3D flow and 2D (shell) structure. Each fluid material can be in contact with multiple fluids, while each flexible structure is restricted to be in contact with only one fluid. c) Schematic view of the vortex generator interaction with nucleate pool boiling with three material domains (two fluids and one bulk solid) and one flexible (fiber) structure.

- ▷ The fluid phases are incompressible.
- ▷ The thin, flexible/rigid structures may not cross material boundaries. That is, the interfacial surface tension forces are strong enough to avoid material interface puncturing by the structure. The physical description of a structure puncturing a material interface is not well-known and not covered in this study (see Fig. 3.a).
- ▷ The thin structures are manifolds of lower dimension than the fluid domain (1D fiber in 2D fluid and 2D shell in 3D fluid).
- ▷ The bulk rigid solid material regions are treated as fluids with prescribed velocity. That is, the thermal dynamics for these regions are resolved without any solid deformation. In this paper, the elastic bulk solids with passive deformation are not considered.
- ▷ The fluid phases can undergo phase-change at their boundaries with other fluids. However, the phase-change at the surface of the flexible structures is excluded in the current work.

In particular, the problem of interest in this study includes several immiscible materials with their associated phase dynamics and their interactions with flexible thin structures. The thin, flexible/rigid structures are modeled using their Lagrangian descriptions. Mathematically, the problem is formulated for three spatial dimensions. A thin structure can be a fiber or a shell. A fiber structure is mathematically one dimensional, very thin in the second dimension, and extended infinitely in the third dimension to accommodate the general description of the problem. The shell structure is mathematically two dimensional, and very thin. The fiber and shell structures are suitable for modeling within 2D and 3D flows, respectively. For example, Fig. 3.a and b show the schematic view of the problem setups with flexible fibers and shells, respectively. Many physical systems may be modeled using this problem setup. For example, energy harvesting [84,85], heat transfer enhancement [86–88], mixing enhancement [89,90], study of polymer flow [91–93], flight of insects [94,95], controlled descent with parachutes [96,97], energy transfer in two-phase heat exchangers [98,99]. Here we use the interaction of active vortex generators (rigid or flexible) with nucleate pool boiling as an example application (Fig. 3.c).

### 3. Governing equations

The governing equations of this study are divided into four categories based on their domain of action, as illustrated in Fig. 3. These are (1) Fluid dynamics (solid colors), (2) Fluid-fluid interfacial dynamics (dashed lines), (3) Solid dynamics (thick solid lines), and (4) Fluid-structure interactions at the fluid-structure interfaces (along the thick solid lines). In the following, the mathematical models of each category are presented.

#### 3.1. Fluid dynamics

The fluid flow with  $N$  phases/materials is modeled with the incompressible Navier-Stokes equations. The level set functions are used to tag the fluid domains and represent the fluid-fluid interfaces. The *material* level set function of  $i$ th material,  $\phi_i$ , is defined as

$$\phi_i(\mathbf{x}, t) = \begin{cases} > 0 & \mathbf{x} \in i\text{th material domain,} \\ \leq 0 & \text{otherwise,} \end{cases} \quad (1)$$

where  $\mathbf{x}$  is the position in space and  $t$  is time. The normal and curvature of the interfaces can be defined based on the *interface* level set,  $\phi_{i,j}(\mathbf{x}, t)$ , between materials  $i$  and  $j$ ,

$$\phi_{i,j}(\mathbf{x}, t) = \begin{cases} > 0 & \mathbf{x} \in \text{ith material domain,} \\ < 0 & \mathbf{x} \in \text{jth material domain,} \\ = 0 & \mathbf{x} \text{ along the interface of ith and jth materials,} \end{cases} \quad (2)$$

$$\mathbf{n}_{i,j} = \frac{\nabla \phi_{i,j}}{|\nabla \phi_{i,j}|}, \quad \kappa_{i,j} = \nabla \cdot \frac{\nabla \phi_{i,j}}{|\nabla \phi_{i,j}|}.$$

Inside each fluid domain, the conservation of mass, momentum, and energy are imposed:

$$\nabla \cdot \mathbf{u} = 0, \quad (3)$$

$$(\rho_i \mathbf{u})_t + \nabla \cdot (\rho_i \mathbf{u} \otimes \mathbf{u} + p_i \mathbb{I}) = \nabla \cdot (2\mu_i \mathbb{D}) + \rho_i \mathbf{g} + \mathbf{f}_f, \quad (4)$$

$$(\rho_i C_{p,i} T)_t + \nabla \cdot (\mathbf{u} \rho_i C_{p,i} T) = \nabla \cdot (k_i \nabla T), \quad (5)$$

for  $\phi_i(\mathbf{x}, t) > 0$ . Here,  $\mathbf{u} = (u, v, w)$  is the velocity vector.  $p_i$ ,  $\rho_i$  and  $\mu_i$  are pressure, density and dynamic viscosity of material  $i$  respectively.  $\mathbf{g}$  is the gravitational acceleration vector,  $\mathbf{f}_f$  is the feedback force density for the fluid-structure interaction, and  $\mathbb{D} = \frac{1}{2}(\nabla \mathbf{u} + (\nabla \mathbf{u})^T)$  is the rate of deformation tensor. In the energy equation,  $T$  denotes the temperature, and  $C_{p,i}$  and  $k_i$  are heat capacity and thermal conductivity of material  $i$  respectively.

### 3.2. Fluid-fluid interaction

The interaction at the fluid-fluid interfaces are represented as proper jump conditions that the fluids must satisfy for mass, momentum, and energy conversations.

► **Mass and energy conservation and phase-change:** The continuity equation, Eq. (3), is only valid in the bulk domain. In order to conserve mass across the interface, the following kinematic jump condition should be applied:

$$[\mathbf{u}] \cdot \mathbf{n}_{i,j} = \dot{m}_{i,j} \left[ \frac{1}{\rho} \right], \quad (6)$$

where  $[x] \equiv x_i - x_j$  and  $\dot{m}_{i,j}$  is inward ( $i$ -to- $j$ ) phase-change mass flux [100]. The velocity of the phase-change interface,  $\mathbf{u}_p$ , can then be found from

$$\mathbf{u}_p \cdot \mathbf{n}_{i,j} = \mathbf{u}_i \cdot \mathbf{n}_{i,j} - \frac{\dot{m}_{i,j}}{\rho_i} = \mathbf{u}_j \cdot \mathbf{n}_{i,j} - \frac{\dot{m}_{i,j}}{\rho_j}. \quad (7)$$

It is assumed that the mass transfer across the interface is linearly related to the energy jump condition [101],

$$\dot{m}_{i,j} = - \frac{[k \nabla T] \cdot \mathbf{n}_{ij}}{L_{i,j}}, \quad (8)$$

where  $L_{i,j}$  is the latent heat of phase-change, and the interface between phase-change materials is assumed to have the prescribed phase-change saturation temperature  $T_p$ . The model is further enhanced to account for specific cases such as the nucleate pool boiling problem (more details in section 4.3).

With the assumption of zero tangential component for  $\mathbf{u}_p$ , the phase-change interface velocity is partitioned into the *advection* and *phase-change* components. The advection part is calculated from the background velocity  $\mathbf{u}_i$ , and the remaining part  $\mathbf{u}_p - \mathbf{u}_i$  defines the phase-change interface velocity in the normal direction:

$$V_p = (\mathbf{u}_p - \mathbf{u}_i) \cdot (-\mathbf{n}_{i,j}) = \frac{\dot{m}}{\rho_i} = \frac{[k \nabla T] \cdot (-\mathbf{n}_{i,j})}{\rho_i L_{i,j}}. \quad (9)$$

This partitioning is advantageous as the advection velocity is divergence-free, while the phase-change velocity may induce volume expansion (or shrinkage) if  $\rho_i \neq \rho_j$ , and can be treated differently.

► **Momentum conservation, capillary force, and viscosity:** The momentum jump condition for the massless interface between  $i$ th and  $j$ th materials is described by

$$[2\mu \mathbb{D} - p \mathbb{I}] \cdot \mathbf{n}_{i,j} = \sigma_{i,j} \kappa_{i,j} \mathbf{n}_{i,j}, \quad (10)$$

where  $\sigma_{i,j}$  is the surface tension coefficient of the interface. To enforce the jump equation, one fluid formulation is adopted for the momentum equation that includes the viscous and surface tension effects for multi-material cases [102],

$$\frac{\partial}{\partial t} (\mathbf{u} H_m) + \nabla \cdot (\mathbf{u} \otimes \mathbf{u}) = - \frac{\nabla p}{\rho} + \frac{\nabla \cdot (2\mu \mathbb{D} H_m)}{\rho} + \mathbf{g} - \sum_{m=1}^N \frac{\gamma_m \kappa_m \nabla H_m}{\rho} + \frac{\mathbf{f}_f}{\rho}, \quad (11)$$

where  $H_m$  is the material color function based on Heaviside function,

$$H_m = H_m(\phi_m) = \begin{cases} 1 & \phi_m \geq 0, \\ 0 & \text{otherwise.} \end{cases} \quad (12)$$

The combined quantities,  $\rho$  and  $\mu$ , are

$$\rho(\mathbf{x}, t) \equiv \sum_{m=1}^N \rho_m H(\phi_m(\mathbf{x}, t)), \quad \mu(\mathbf{x}, t) \equiv \sum_{m=1}^N \mu_m H(\phi_m(\mathbf{x}, t)), \quad (13)$$

and  $\gamma_m$  is defined based on the surface tension coefficients. For  $N = 3$  those are defined as

$$\gamma_1 = \frac{\sigma_{12} + \sigma_{13} - \sigma_{23}}{2}, \quad \gamma_2 = \frac{\sigma_{12} + \sigma_{23} - \sigma_{13}}{2}, \quad \gamma_3 = \frac{\sigma_{13} + \sigma_{23} - \sigma_{12}}{2}, \quad (14)$$

and would satisfy a multi-material junction equilibrium formation, known as the Neumann's triangle [103]:

$$\frac{\sin(\theta_1)}{\sigma_{23}} = \frac{\sin(\theta_2)}{\sigma_{13}} = \frac{\sin(\theta_3)}{\sigma_{12}}. \quad (15)$$

See Fig. 4.a for a depiction of corresponding surface tension coefficients and contact angles.

▷ **Interface evolution:** The motion of the interface is governed by the advection of material color function:

$$(H_m)_t + \mathbf{v}_{\text{ext}} \cdot \nabla H_m = 0, \quad (16)$$

where  $\mathbf{v}_{\text{ext}}$  is calculated by the extending the interface velocity to the region around the material interface. The velocity field  $\mathbf{v}_{\text{ext}}$  consists of the background fluid velocity  $\mathbf{u}$ , and phase-change velocity  $-V_p \mathbf{n}_{i,j}$ . The fluid velocity is defined in the whole domain, and evaluation and extension of phase-change velocity is explained in phase-change part of subsection 4.3.

### 3.3. Structural dynamics

Here we limit the definition of a thin structure to an elastic fiber geometry or a flexible shell body with a negligible thickness ( $h_s$ ).

▷ **Fiber structures:** The fiber geometry is assumed to be elastic with its dynamics governed by

$$m_e \frac{\partial^2 \mathbf{X}}{\partial t^2} = \frac{\partial}{\partial s} (\sigma \mathbf{t} + q \mathbf{n}) - \mathbf{F}_s, \quad (17)$$

where  $s$  is a Lagrangian coordinate chosen to be the arc length along the fiber ( $0 \leq s \leq L_s$ ),  $\mathbf{X} = \{x, y\}$  describes the material position of the fiber,  $\mathbf{t} = \frac{\partial \mathbf{X}}{\partial s}$  is the unit tangent vector along the coordinate  $s$ , and  $\mathbf{n}$  is the unit normal vector. Furthermore,  $m_e$  is the excess mass per unit area of the structure, defined as  $m_e = m_s - \rho_f h_s$ , where  $m_s$  is the mass per unit length of the thin structure,  $\rho_f$  is the density of the fluid, and  $h_s$  denotes the thickness of the fiber. Note that the area here is defined based on the length of the fiber and the unit depth in the third dimension. On the right-hand side of the equation,  $\sigma$  is the tension, and  $q$  is the transverse stress, and  $\mathbf{F}_s$  is the force density applied by the fiber on the surrounding fluid. For an extensible fiber, tension is related to the stretching in the structure with  $\sigma = k_s (|\frac{\partial \mathbf{X}}{\partial s}| - 1)$ . Also for very large  $k_s$  range, an inextensibility constraint expressed as  $\frac{d}{dt} |\frac{\partial \mathbf{X}}{\partial s}| = 0$  is employed to calculate the tension  $\sigma$ :

$$\frac{\partial^2}{\partial s^2} (\sigma \mathbf{t}) \cdot \mathbf{t} = \frac{m_e}{2} \frac{\partial^2}{\partial t^2} (\mathbf{t} \cdot \mathbf{t}) - m_e \frac{\partial \mathbf{t}}{\partial t} \cdot \frac{\partial \mathbf{t}}{\partial t} - \frac{\partial}{\partial s} \left( \frac{\partial(q\mathbf{n})}{\partial s} - \mathbf{F}_s \right). \quad (18)$$

Using the Euler-Bernoulli assumption for a slender nearly inextensible fiber ( $M = k_b \kappa$ , with  $M$  the elastic moment along the fiber,  $k_b$  the bending rigidity, and  $\kappa = -\frac{\partial^2 \mathbf{X}}{\partial s^2}$  the local curvature along the plate), the transverse stress  $q$  becomes:

$$q = \frac{\partial M}{\partial s} = -\frac{\partial}{\partial s} \left( k_b \frac{\partial^2 \mathbf{X}}{\partial s^2} \right) \cdot \mathbf{n}. \quad (19)$$

The free boundary condition of the fiber is enforced by imposing  $\partial^2 \mathbf{X} / \partial s^2 = 0$  and  $\partial^3 \mathbf{X} / \partial s^3 = 0$ . The fixed edge is modeled with  $\mathbf{X} = \mathbf{X}_0$  and  $\partial \mathbf{X} / \partial s = \partial \mathbf{X}_0 / \partial s$ . In case of a pinned boundary condition, the later boundary condition is changed to  $\partial^2 \mathbf{X} / \partial s^2 = 0$ .

▷ **Shell structures:** The equation of motion for the shell structures are written based on the curvilinear coordinate system of the shell surface ( $0 \leq s_1 \leq L_s, 0 \leq s_2 \leq W_s$ ), in three dimensional space  $\mathbf{X} = \{x, y, z\}$  as [104,105]:

$$m_e \frac{\partial^2 \mathbf{X}}{\partial t^2} = \sum_{i,j=1}^2 \left[ \frac{\partial}{\partial s_i} \left( \sigma_{ij} \frac{\partial \mathbf{X}}{\partial s_j} \right) - \frac{\partial^2}{\partial s_i \partial s_j} \left( k_b \frac{\partial^2 \mathbf{X}}{\partial s_i \partial s_j} \right) \right] - \mathbf{F}_s, \quad (20)$$



where  $m_e = m_s - \rho_f h_s$  is the excess mass of the shell per unit area,  $h_s$  denotes the cross sectional thickness of the shell,  $\rho_f$  is the density of the surrounding fluid,  $k_b = \frac{Eh_s^3}{12(1-\nu^2)}$  is the bending coefficients, and  $\sigma_{ij}$  are the in-plane forces, defined as

$$\sigma_{11} = \phi_{11} \left( \frac{\partial \mathbf{X}}{\partial s_1} \cdot \frac{\partial \mathbf{X}}{\partial s_1} - 1 \right), \quad \sigma_{22} = \phi_{22} \left( \frac{\partial \mathbf{X}}{\partial s_2} \cdot \frac{\partial \mathbf{X}}{\partial s_2} - 1 \right), \quad \sigma_{12} = \sigma_{21} = \phi_{12} \frac{\partial \mathbf{X}}{\partial s_1} \cdot \frac{\partial \mathbf{X}}{\partial s_2}, \quad (21)$$

$$\phi_{11} = \phi_{22} = \frac{Eh_s}{1-\nu^2}, \quad \phi_{12} = \frac{Eh_s}{1-\nu^2} \frac{1-\nu}{2}, \quad (22)$$

where  $E$  and  $\nu$  are the Young's modulus and Poisson's ratio of the shell material respectively. The boundary conditions of the shell structure at different edges, for example along the  $s_1 = 0$  edge, are specified for different type of boundaries. For the fixed boundary condition:  $\mathbf{X} = \mathbf{X}_0$  and  $\partial^2 \mathbf{X} / \partial s_1^2 = 0$ ; for the free boundary condition:  $\partial^2 \mathbf{X} / \partial s_1^2 = 0$ ,  $\partial^3 \mathbf{X} / \partial s_1^3 = 0$ ,  $\sigma_{ij} = 0$ , and  $k_b = 0$ .

### 3.4. Fluid-structure interaction

The fluid-structure interaction is modeled as a feedback forcing term [32,36] in right hand sides of Eqs. (17) and (20):

$$\mathbf{F}_s = -\alpha \int_0^t (\mathbf{U}_f - \mathbf{U}_s) d\tau - \beta (\mathbf{U}_f - \mathbf{U}_s), \quad (23)$$

where  $\mathbf{U}_f$  is the fluid velocity interpolated at the surface of the structure, and  $\mathbf{U}_s$  is the structure velocity defined as  $\mathbf{U}_s = d\mathbf{X}/dt$ ,  $\alpha$  and  $\beta$  are positive coefficients essentially representing the stiffness of a spring between two Lagrangian points: one moves with the structure and the other one moves with the interpolated local flow velocity. The Lagrangian fluid velocity at the structure surface is interpolated from the Eulerian fluid velocity in the bulk region using a Dirac delta kernel function,

$$\mathbf{U}_f(s, t) = \int_{\Omega_f} \mathbf{u}(\mathbf{x}, t) \delta(\mathbf{X}(s, t) - \mathbf{x}) d\mathbf{x}, \quad (24)$$

and the Eulerian fluid body force in bulk region is calculated from the structure's Lagrangian force according to:

$$\mathbf{f}_f(\mathbf{x}, t) = \int_{\Omega_s} \mathbf{F}_s(s, t) \delta(\mathbf{X}(s, t) - \mathbf{x}) ds. \quad (25)$$

Here we make some notes to have a consistent definition of quantities for fiber and shell geometries. The units for the fluid force density  $\mathbf{f}_f$  is  $ML^{-2}T^{-2}$ , while the units for the force density of the fiber and shell structure  $\mathbf{F}_s$  is  $ML^{-1}T^{-2}$ . The definition of the structure coordinate variable  $\mathbf{s} = \{s_1, s_2\}$  is obvious for a shell structure. However, for a fiber structure, one can think of it as  $\mathbf{s} = s = s_1$ , and  $s_2$  as the coordinate in the extension direction to emulate the fiber geometry in the three-dimensional space. The delta function  $\delta(\mathbf{s}, t)$  is defined in three dimensional space with unit  $L^{-3}$ . For the fiber structure, the convolution integral over the extension dimension reduces to 1 with unit  $L$ , and the rest of the integral operation may be evaluated within the two-dimensional space as described in the numerical implementation in the next chapter.

Regarding the force-feedback method it is important to note the following points:

- ▷ When the values of  $\alpha$  and  $\beta$  are picked properly to enforce a satisfactory feedback force, making the velocity continues across the fluid-structure interface, the jump in stress across the interface is applied implicitly (proof by Peskin and Printz [106]). That is, for fluid stress tensor  $\mathbb{T} = \nabla \cdot (-p\mathbb{I} + 2\mu\mathbb{D})$ , and stress jump condition  $[\mathbb{T}_{ij}]n_j = -F_i/|\partial X/\partial s|$  we get:

$$[p] = -n_i [\mathbb{T}_{ij}]n_j = \frac{\mathbf{F} \cdot \mathbf{n}}{|\partial X/\partial s|}, \quad \mu_i \mathbf{t} \cdot \left[ \frac{\partial \mathbf{u}}{\partial n} \right] = t_i [\mathbb{T}_{ij}]n_j = -\frac{\mathbf{F} \cdot \mathbf{t}}{|\partial X/\partial s|}. \quad (26)$$

The factor  $|\partial X/\partial s|$  appears in the denominator for the Lagrangian to Eulerian transformation of the structural force, that is, for the general extensible case where  $s$  is not the arc length ( $\mathbf{t} = (\partial \mathbf{X}/\partial s)/|\partial \mathbf{X}/\partial s|$ ). Depending on the order of accuracy needed by the algorithms, higher order jump conditions may be included as well [107,108].

- ▷ Although the formulation here is for the "thin" structures, this approach can be used for stationary volumetric structures as well. See Appendix A for the flow around a rigid stationary cylinder test.



#### 4. Numerical methods

The applied partitioning method for the FSI problems facilitates the solution of the fluid and structure with the minimal interconnection of the solvers. The numerical algorithm to solve the multi-material/multi-phase fluid system is based on operator splitting and explicit in time, while the structural dynamics are solved implicitly. The algorithm procedures are applied in the following order.

- ▷ **Structure solution and fluid-structure interaction:** The fluid velocity is interpolated to the solid nodes, and the feedback force is calculated. The structural equations are solved, and the position and velocity of the structural points are evaluated at the next time step. The feedback force term is interpolated back to the fluid grid to be included in the solution of the momentum equation.
- ▷ **Advection:** An interface reconstruction is calculated and the distribution of mass, momentum and energy, Eqs. (3), (4) and (5), are evaluated using cell integrated semi-Lagrangian (CISL) methods [109,110]. The exact signed distance function is calculated exactly from the reconstructed interfaces.
- ▷ **phase-change:** The mass transfer due to the phase-change is evaluated, along with the updated distance function, volume fractions, and cell centroids.
- ▷ **Viscosity and surface tension:** The viscous force in Eq. (4) and temperature diffusion in Eq. (5) are evaluated. The surface tension force term is determined from the updated interfaces.
- ▷ **Pressure Projection:** A projection step is applied to evaluate the pressure force and update the flow velocity vector.

Here, we briefly describe the numerical methods, while more detailed information is referred to other papers by authors [82,109,110]. While the descriptions and depictions are given in two spatial dimensions for brevity, the extension to three-dimensional space is straight-forward as we have presented in the test problems. It is worth mentioning that the following aspects are new contribution compared to the works mentioned above:

- ▷ Fluid-structure interaction in multi-material multi-phase systems.
- ▷ Finding a heuristic stability criteria for the fluid-structure interaction algorithm with the combination of  $\alpha$ ,  $\Delta s$ , and  $\Delta t$ .
- ▷ Applying the continuous moment-of-fluid technique to reach a more robust interface reconstruction in the presence of large surface tension forces.

##### 4.1. Fluid and structure grids

The fluid equations are solved on a uniform rectangular staggered Cartesian grid. A computational cell,  $\Omega_{i,j}$ , is defined as,

$$\Omega_{i,j} = \left\{ \mathbf{x} : x \in \left[ x_i - \frac{\Delta x}{2}, x_i + \frac{\Delta x}{2} \right], y \in \left[ y_i - \frac{\Delta y}{2}, y_i + \frac{\Delta y}{2} \right] \right\}, \quad (27)$$

where  $\mathbf{x}_{i,j} = \{x_i, y_j\}$  is the center of the cell  $\Omega_{i,j}$ . The domain of material  $m$  in a cell at time  $t^n$  is denoted by  $\Omega_{m,i,j}^n$ , and the zeroth and first order moments of the  $m$ th material distribution, corresponding to the volume fraction and centroid position, are defined as,

$$F_{m,i,j}^n = \frac{\int_{\Omega_{m,i,j}^n} d\Omega}{V_{i,j}}, \quad \mathbf{x}_{m,i,j}^{c,n} = \frac{\int_{\Omega_{m,i,j}^n} \mathbf{x} d\Omega}{V_{m,i,j}^n}, \quad (28)$$

where  $V_{i,j}$  is volume of the  $(i, j)$  computational cell, and  $V_{m,i,j}^n$  is volume of the portion for material  $m$  in the computational cell ( $V_{i,j} = \sum_m V_{m,i,j}$ ). Here, the velocity components are defined on the face centers, while other variables such as pressure and temperature are defined on the cell centers (see Fig. 4.a-b).

For evaluation of the structural dynamics, we employ curvilinear structural grids along  $\mathbf{s}$ . All the structural variables are defined on the node vertices (shown with subscript  $i$ ), except the solid tension, which is defined on the centroid of the grid cells (shown with subscript  $\hat{i}$ ). The grid spacing of structure  $\Delta s$  is set be smaller than the fluid grid's spacing. Here we use  $\Delta s \approx 0.8 \Delta x$  (see Fig. 4.c). The number of cells for the structure discretization is denoted by  $n_s$ .

The discretization of the fluid dynamics on the Cartesian grid enables us to use a straight-forward adaptive mesh refinement (AMR) algorithm for solving the flow dynamics [109]. In the current model, mesh refinement is only applied to the fluid grid, and the structure grid refinement does not change. The refinement criteria for the AMR algorithm tag the cells occupied by the structures and keep them in the finest refinement level. Therefore, the interface between the fluid and solid in the FSI algorithm is resolved consistently with the same ratio between  $\Delta x_{\text{finest}}$  for the fluid and  $\Delta s$  for the structure.

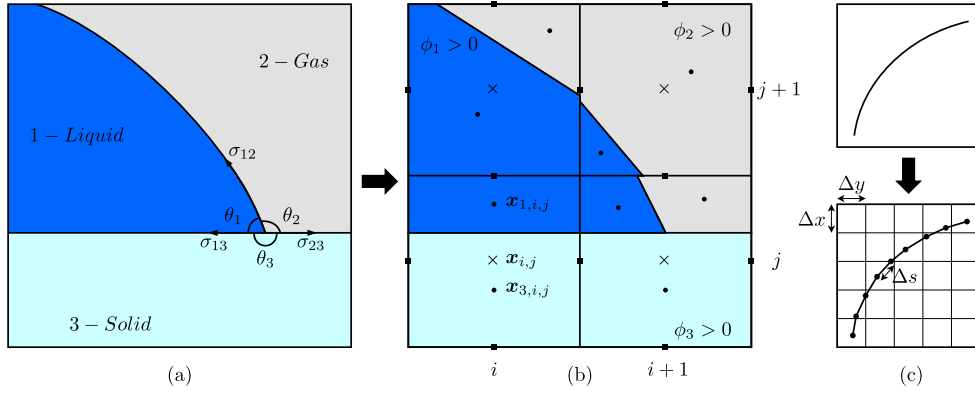


**Fig. 4.** (a) Physical domain: region near a triple point. Surface tension forces are at equilibrium, determining the contact angles. (b) Discretized domain: crosses show cell centers, circles represent cell centroids, and squares depict the face-center grid points in each cell. (c) Discretization of a fiber structure.

#### 4.2. Interface reconstruction

The material volume fractions and centroids are used to calculate a piecewise linear reconstruction to the interface. In a multi-material computational cell, the reconstructed interface is a line in 2D or a plane in 3D problem domains. The continuous moment-of-fluid (CMOF) method employed here, in contrast to other moment-of-fluid (MOF) reconstruction method [10,18], adopts a larger non-local stencil to define the reference moment of the materials in each cell. This procedure, which may resemble the addition of artificial surface tension, produces a smoother and more accurate reconstructed interface for problems with significant surface tension.

In the CMOF method, a super-cell is defined by expanding the current computational cell in all directions by one grid cell (Fig. 5.a):

$$\Omega_{i,j}^s = \left\{ \mathbf{x} : x \in \left[ x_i - \frac{3\Delta x}{2}, x_i + \frac{3\Delta x}{2} \right], y \in \left[ y_i - \frac{3\Delta y}{2}, y_i + \frac{3\Delta y}{2} \right] \right\}. \quad (29)$$

The centroid of the super-cell  $\mathbf{x}_{m,i,j}^{s,n}$  is the weighted average of the centroid in the super-cell,

$$\mathbf{x}_{m,i,j}^{s,n} = \frac{\sum_{i,j} F_{m,i,j}^n \mathbf{x}_{m,i,j}^{c,n} V_{i,j}}{\sum_{i,j} F_{m,i,j}^n V_{i,j}}. \quad (30)$$

The reconstructed interface ( $b, \mathbf{n}$ ) is found by matching the volume fraction of the reconstruction to the reference value, ( $F_{\text{rec}} = F_{\text{ref}}$ ), while minimizing the error of the centroid location

$$E_{\text{rec}} = \|\mathbf{x}_{\text{ref}}^c - \mathbf{x}_{\text{rec}}^c(\mathbf{n}, b)\|_2. \quad (31)$$

For the CMOF method, we set the reference volume fraction from the center cell,  $F_{\text{ref}} = F_{m,i,j}^n$ , so the reconstruction is volume conservative, and the reference centroid from the super-cell,  $\mathbf{x}_{\text{ref}}^c \equiv \mathbf{x}_{m,i,j}^{s,n}$  (Fig. 5.b).

The material interface reconstruction for a multi-material cell is done through an iterative procedure. The process starts from a complete cell and repeats the reconstruction process iteratively for the uncaptured regions to generates a volume-preserving reconstruction at multi-material cells (see Fig. 5.c). Upon compilation of the reconstruction, the identified interfaces are used to recalculate the level set functions as an exact signed distance values.

#### 4.3. Fluid solver

An operator splitting technique is used to solve for the advection, diffusion, viscous, surface tension, phase-change dynamics of the flow:

► **Advection:** The fluid advection is performed using the directionally split cell integrated semi-Lagrangian (CISL) method and the conservative approach proposed by Weymouth and Yue [111]. Here the mass advection, Eq. (16), is transformed to spatially split advection steps for the volume fraction in pseudo time step  $\tau$  [111]. For example the resultant system of equations in 2D is:

$$\begin{aligned} (F_m)_\tau + (uF_m)_x &= 0, & 0 \leq \tau \leq \Delta t & \quad \text{if } F_{m,i,j} < 0.5, \\ (F_m)_\tau + (vF_m)_y &= 0, & \Delta t \leq \tau \leq 2\Delta t & \end{aligned} \quad (32)$$

$$\begin{aligned} (F_m)_\tau + (uF_m)_x &= (u)_x, & 0 \leq \tau \leq \Delta t & \quad \text{if } F_{m,i,j} \geq 0.5. \\ (F_m)_\tau + (vF_m)_y &= (v)_y, & \Delta t \leq \tau \leq 2\Delta t & \end{aligned} \quad (33)$$

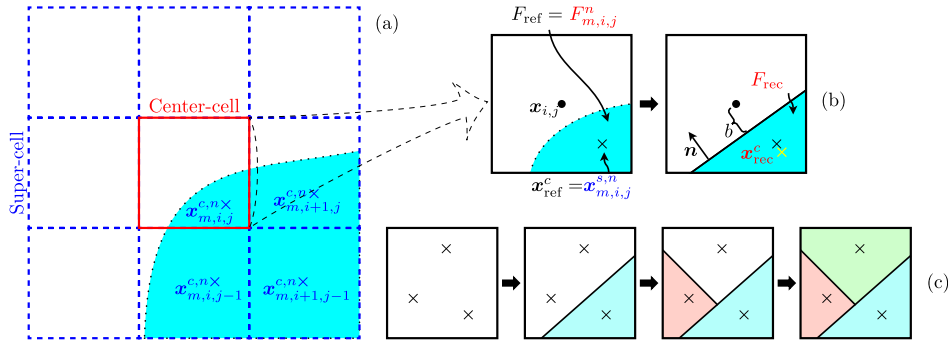


**Fig. 5.** (a) The center-cell and super-cell around it for CMOF reconstruction. The actual material interface is shown with dotted line. (b) Reference volume fraction and centroid and corresponding reconstructed planer interface represented as  $\Omega_{i,j} \cap \{\mathbf{x} | \mathbf{n} \cdot (\mathbf{x} - \mathbf{x}_{i,j}) + b = 0\}$ . (c) Volume-tessellating nested dissection based on CMOF reconstruction. The crosses are material centroids. White spaces are the unoccupied regions. Three material domains are shown with different colors. (For interpretation of the colors in the figure(s), the reader is referred to the web version of this article.)

The backward characteristic tracing method by Weymouth and Yue [111] is employed to solve Eq. (32) and the complement problem of Eq. (33) namely solving for  $(F_{m,i,j})^{\text{comp}} = 1 - F_{m,i,j} < 0.5$ . Here, we describe the algorithm for the  $x$  direction while other spatial directions are also similar. With the known tessellating reconstruction at time  $t^n$ , the boundaries of this region,  $x_{i+1/2}$  and  $x_{i-1/2}$ , are traced backed using the face-centered characteristic velocities  $u_{i+1/2,j}$  and  $u_{i-1/2,j}$  to find the boundaries of the departure region  $x_{\text{right}}$  and  $x_{\text{left}}$  (Fig. 6.a).

$$\Omega_{i,j}^{\text{target}} = \Omega_{i,j}, \quad (34)$$

$$x_{\text{right}} = x_{i+1/2} - \Delta t u_{i+1/2,j}, \quad x_{\text{left}} = x_{i-1/2} - \Delta t u_{i-1/2,j}, \quad (35)$$

$$\Omega_{i,j}^{\text{depart}} = (T_{i,j}^{\text{CISL}})^{-1}(\Omega_{i,j}^{\text{target}}) = \{\mathbf{x} : x \in [x_{\text{left}}, x_{\text{right}}], y \in [y_i - \Delta y/2, y_i + \Delta y/2]\}, \quad (36)$$

where the mapping function for this transformation is defined as:

$$T_{i,j}^{\text{CISL}}(x, y) = (\alpha x + \beta, y) : \Omega_{i,j}^{\text{depart}} \rightarrow \Omega_{i,j}^{\text{target}}, \quad \text{with } \alpha = \Delta x / (x_{\text{right}} - x_{\text{left}}), \beta = x_{i-1/2} - \alpha x_{\text{left}}. \quad (37)$$

The intersection of the departure region and the domain of material  $m$  in cells  $\{i-1, j\}, \{i, j\}$  and  $\{i+1, j\}$  at time  $t^n$  can be calculated as:

$$V_{i',i,j}^n = \Omega_{m,i+i',j}^n \cap \Omega_{i,j}^{\text{depart}}, \quad i' = -1, 0, 1. \quad (38)$$

The transformation of these departure regions using the mapping function  $T_{i,j}^{\text{CISL}}$  gives the corresponding partitions in the target region (Fig. 6.b),

$$V_{i',i,j}^{n+1} = T_{i,j}^{\text{CISL}}(\Omega_{m,i+i',j}^n) \cap \Omega_{i,j}^{\text{target}}, \quad i' = -1, 0, 1. \quad (39)$$

This follows by updating the volume fraction and centroid position of the cell  $\{i, j\}$  as

$$\tilde{F}_{i,j}^x = \frac{\sum_{i'=-1}^1 |V_{i',i,j}^n|}{|\Omega_{i,j}|}, \quad \tilde{\mathbf{x}}_{i,j}^{c,x} = \frac{\sum_{i'=-1}^1 \int_{V_{i',i,j}^{n+1}} \mathbf{x} d\mathbf{x}}{\tilde{F}_{i,j}^x |\Omega_{i,j}|}. \quad (40)$$

The interface is reconstructed using the updated volume fractions and centroids after each directional sweep, and the updated volume fractions and centroids are used as  $F$  and  $\mathbf{x}^c$  for the next directional sweep. Similar algorithms are used for advection operators in momentum and energy equations [110].

- ▷ **Phase-change:** In the presence of the phase-change between materials  $m_1$  and  $m_2$ , the interface between materials move with the normal velocity  $V_p$  (see Section 3.2) with the advection-expansion process. In this case, the phase-change velocity is first calculated using the jump condition Eq. (9) for cells in a band around the interface between material  $m_1$  and  $m_2$ . For a cell  $\{i, j\}$  in the band we find the closet point on the interface:

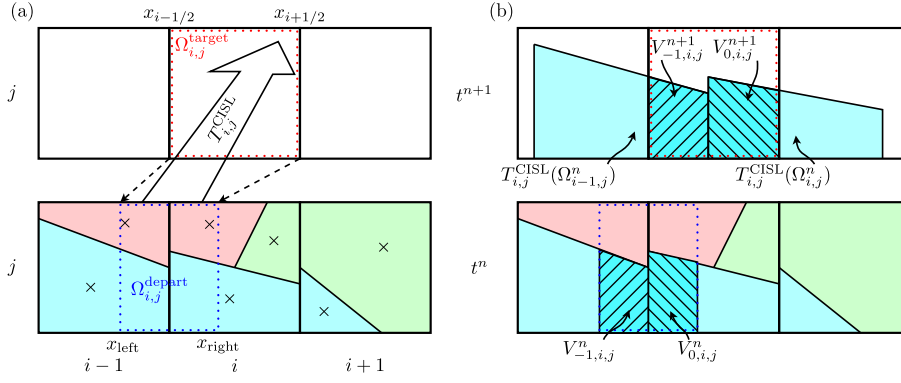


**Fig. 6.** CISL method for mass distribution and centroid position. The backward characteristic tracing in  $x$  direction is shown for the blue (which covers the lower left and mid-bottom regions) material. (a) Material distribution, centroid position (x) and interface reconstruction for cells  $\{i-1, j\}$ ,  $\{i, j\}$  and  $\{i+1, j\}$  at time  $t^n$ , and target region at time  $t^{n+1}$  are shown. With backward characteristic tracing, the mapping function is calculated. (b) Transformation of the material domain using the mapping function and finding the intersection with the target region. The accumulated materials in the target region give of the volume fraction and centroid of advected material into the target region.

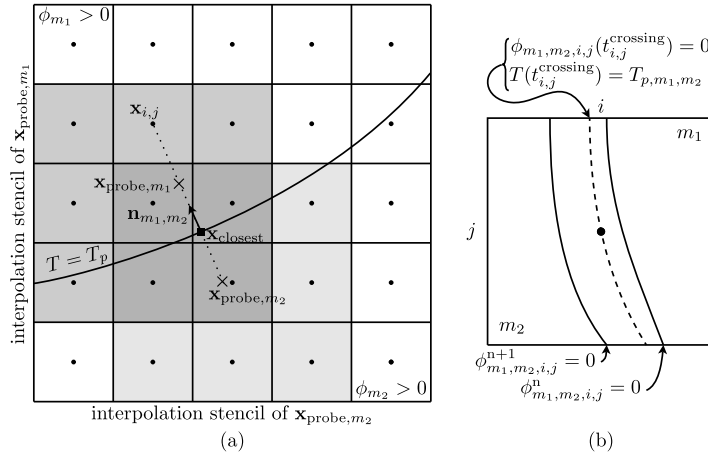


**Fig. 7.** a) Calculation of the temperature gradient in the front normal direction on a phase-change interface. b) Progress of the phase-change front and occurrence of a phase-change cell. At time  $t^n$  center of the cell  $\{i, j\}$  is in the domain of material  $m_2$  and the temperature  $T_{i,j}^n$  represent the temperature in material  $m_2$ . To have a consistent time integration centered at the cell centers and corresponding the material that occupies the cell center at time  $t^{n+1}$  the crossing time for the center of the phase-change cell is found and the temporal discretization is modified accordingly.

$$\mathbf{x}_{\text{closest}} = \mathbf{x}_{i,j} - \phi_{m_1,m_2} \mathbf{n}_{m_1,m_2}. \quad (41)$$

Two intercept points are found by extending  $\mathbf{x}_{\text{closest}}$  in the front normal direction into each material with distance  $h = \min(\Delta x, \Delta y)$ . The temperature in these intercept points are interpolated from the cells in a  $3 \times 3$  stencil around in each domain (only cells with  $F_{m_k} > 0$  when interpolating in the domain of material  $m_k$ ). The temperature gradient is evaluated, knowing the temperature of the phase-change interface (see Fig. 7.a),

$$\nabla T_{m_1} = \frac{T_{\text{probe},m_1} - T_{p,m_1,m_2}}{h} \mathbf{n}_{m_1,m_2}, \quad \nabla T_{m_2} = -\frac{T_{\text{probe},m_2} - T_{p,m_1,m_2}}{h} \mathbf{n}_{m_1,m_2}. \quad (42)$$

A similar approach has been previously employed for the solidification phase-change process and verified with a theoretical solution [75]. The boiling process, however, requires a slightly more involved approach. In this case, the overall mass transfer of a vapor bubble in contact with a hot substrate heavily relies on the material and thermal dynamics at the triple point, and the discretization explained above requires modification near a triple point to evaluate a better estimation of  $\nabla T$ . In addition, a liquid film may form at the triple point and propagate under the contact region of the vapor bubble, creating a microlayer on the interface, which greatly alters the local large heat flux. To model this micro-region, with a potentially high-temperature gradient, we employ the technique developed by Stephan and Busse [112], which along with its variations [60,113,114] have shown agreeable results for prediction of the boiling rate of the vapor bubble.

A macro-micro region model is assumed near a triple point with a linearly varying thermal layer between the substrate and boiling saturation temperatures. A local coordinate system  $(\psi, \chi)$  is defined near the triple point as shown

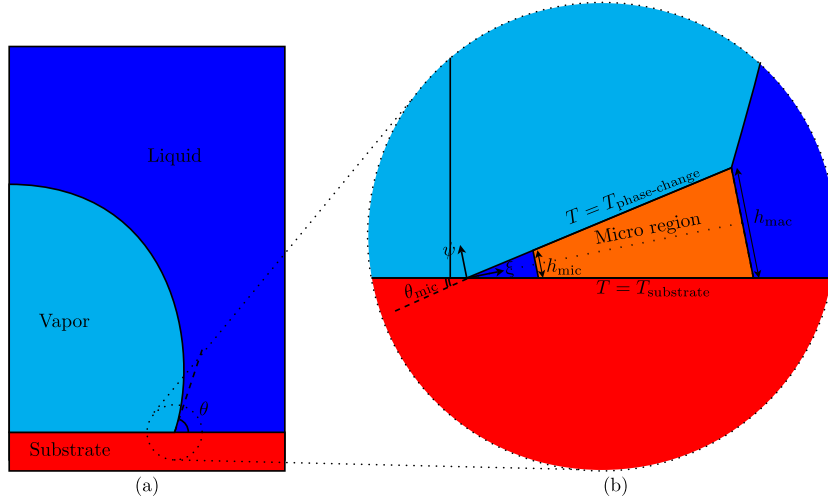


**Fig. 8.** (a) Macro-model near the triple point during boiling: Vapor bubble is in contact with the substrate at the triple point. (b) Micro-region model: A film of liquid slides under the contact point and enhance the phase-change rate.

in Fig. 8. The temperature in micro-region  $T(\psi, \xi)$ , and location of vapor-liquid interface  $\eta(\xi)$  can then be calculated as:

$$T(\psi, \xi) = \frac{T_p \psi + (\eta(\xi) - \psi)(T_p + T_s)/2}{\eta(\xi)}, \quad \eta(\xi) = \xi \tan(\theta_{\text{mic}}/2), \quad (43)$$

where  $T_p$  and  $T_s$  are the phase-change and substrate temperatures, respectively, and  $\theta_{\text{mic}}$  is the contact angle of the microlayer. The temperature gradient is normal to the liquid-vapor interface can be obtained as:

$$\nabla T \cdot \mathbf{n} = |\nabla T| = \left| \frac{T_p - T_s}{2\xi \tan(\theta_{\text{mic}}/2)} \begin{pmatrix} 1 \\ \tan(\theta_{\text{mic}}/2) \end{pmatrix} \right| = \frac{(T_p - T_s)\sqrt{1 + \tan^2(\theta_{\text{mic}}/2)}}{2\xi \tan(\theta_{\text{mic}}/2)}. \quad (44)$$

Let  $\psi = \xi \tan(\theta_{\text{mic}}/2)$ , the average of  $\nabla T \cdot \mathbf{n}$  along the vapor-liquid in the micro-region is

$$\overline{\nabla T \cdot \mathbf{n}}_{\text{mic}} = \frac{(T_p - T_s)\sqrt{1 + \tan^2(\theta_{\text{mic}}/2)}}{h_{\text{mac}} - h_{\text{mic}}} \ln \left( \frac{h_{\text{mac}}}{h_{\text{mic}}} \right). \quad (45)$$

The micro-model involves three main parameters,  $h_{\text{mic}}$ ,  $h_{\text{mac}}$ , and  $\theta_{\text{mic}}$ , that are required to be adjusted based on the experimental observation and physical assumptions. It is evident that the value for  $h_{\text{mic}}$  should be greater than zero. Here, tentatively, a value corresponding to the diameter of a few liquid molecules is chosen. The value of  $h_{\text{mac}}$ , on the other hand, is set to be the minimum distance over which the temperature gradient can be computationally resolved away from the triple point (twice the grid size covering the triple point region). Finally,  $\theta_{\text{mic}}$  is chosen to be equal or less than the apparent contact angle, which can be found from the surface tension coefficients from

$$\theta = \cos^{-1} \left( \frac{\sigma_{\text{v,b}} - \sigma_{\text{l,b}}}{\sigma_{\text{v,l}}} \right). \quad (46)$$

The volume expansion due to phase-change, Eq. (6), is explicitly expressed using the Dirac delta function:

$$\nabla \cdot \mathbf{u} = \dot{m}_{m_1, m_2} \left[ \frac{1}{\rho} \right] \delta_{m_1, m_2}, \quad (47)$$

where the Dirac delta function  $\delta_{m_1, m_2}$  is non-zero only on the interface between materials  $m_1$  and  $m_2$ . This expansion term can be discretized for the cell-centered divergence term evaluated from

$$\nabla \cdot \mathbf{u}_{i,j} = E_{m_1, m_2; i, j} = \frac{\Delta F_{m_1, m_2; i, j}}{\Delta t} \rho_{m_1} \left[ \frac{1}{\rho} \right], \quad (48)$$

where  $\Delta F_{m_1, m_2; i, j}$  is the change of volume fraction in cell  $i, j$  due to the phase-change. In Eq. (48), the volume expansion is enforced in the domain of material  $m_2$  (that is, the movement of phase-change front in domain of material  $m_1$  needs no correction). An unsplit CISL technique similar to the algorithm described previously for the advection is used to evolve the domain due to the phase-change.

- ▷ **Diffusion:** The diffusion operator in the energy equation, Eq. (5), is discretized using the second-order central difference in space and backward Euler method in time. The temperature boundary condition on a phase-change interface is applied with the modified discretization on cells with phase-change. For example, in the case of Dirichlet boundary condition  $T = T_{p,m_1,m_2}$  on  $\phi_{m_1,m_2} = 0$ , the known temperature is applied by anchoring the temperature on a cell center that lays on the path of the phase-change front. That is,  $\phi_{m_1,m_2}^n < 0$  and  $\phi_{m_1,m_2}^{n+1} > 0$ , meaning that the center of the cell is swept by phase-change front during this time step. The crossing time of the phase-change front at the cell-center position (Fig. 7.b) can be found from

$$t_{i,j}^{\text{crossing}} = \frac{|\phi_{m_1,m_2,i,j}^{n+1}|t^n + |\phi_{m_1,m_2,i,j}^n|t^{n+1}}{|\phi_{m_1,m_2,i,j}^{n+1}| + |\phi_{m_1,m_2,i,j}^n|}, \quad (49)$$

and be used to evaluate a modified temporal discretization of the phase-change cell as,

$$\rho_{m_1} C_{p,m_1} \frac{T_{m_1,i,j}^{n+1} - T_{p,m_1,m_2}}{t^{n+1} - t_{i,j}^{\text{crossing}}} = \nabla \cdot k_{m_1} \nabla T_{i,j}^{n+1}. \quad (50)$$

- ▷ **Viscosity:** The viscous term  $\nabla \cdot (2\mu_i \mathbb{D})$  is evaluated using an implicit BiCGSTAB method with Jacobi preconditioner and red-black Gauss-Seidel decoupled smoother [115].
- ▷ **Surface tension:** The surface tension term,

$$\mathbf{f}_{\text{tens}} = - \sum_{m=1}^N \frac{\gamma_m \kappa_m \nabla H_m}{\rho}, \quad (51)$$

is discretized on the cell faces (MAC grid points). For example, for the face  $\{i + 1/2, j\}$  it is

$$f_{\text{tens},i+1/2,j,m}^{\text{MAC}} = - \frac{\gamma_m \kappa_{i+1/2,j,m} (H(\phi_{i+1,j,m}) - H(\phi_{i,j,m}))}{\rho_{i+1/2,j,m}^{n+1} \Delta x}. \quad (52)$$

The weighted average of surface tension force at the cell centers is calculated using the density at the face centers as weighting coefficients [116]. If only two materials are present in the cell, the curvature is evaluated using the level set height function method [117,118]. Otherwise, the curvature is evaluated based on the divergence of interface normal,  $\kappa_m = \nabla \cdot \mathbf{n}_m$ , discretized on the neighboring nodes of the cell center. If a solid material is present in a multi-material cell, the fluid-fluid interfaces are extended into a solid region based on the known contact angle and used to evaluate the curvature. The details of these procedures are given in [119].

- ▷ **Pressure projection:** A pressure projection method is used to calculate the divergence-free velocity field at the next time step. The effects of viscous ( $\mathbf{f}_{\text{visc}}$ ), surface tension ( $\mathbf{f}_{\text{tens}}$ ), and FSI forces ( $\mathbf{f}_f$ ), and gravity ( $\mathbf{g}$ ) are included to the velocity after advection and phase-change update:

$$\mathbf{u}^* = \mathbf{u}_{\text{adv-phc}} + \Delta t (\mathbf{f}_{\text{visc}} + \mathbf{f}_{\text{tens}} + \mathbf{f}_f + \mathbf{g}). \quad (53)$$

The velocity at the next time step is calculated from

$$\mathbf{u}^{n+1} = \mathbf{u}^* - \Delta t \frac{\nabla p^{n+1}}{\rho}, \quad (54)$$

where the pressure satisfies

$$\nabla \cdot \frac{\nabla p^{n+1}}{\rho} = \frac{\nabla \cdot \mathbf{u}^*}{\Delta t} - \begin{cases} \frac{\bar{E}}{\Delta t}, & \text{in cells with phase-change,} \\ 0 & \text{otherwise.} \end{cases} \quad (55)$$

The BiCGSTAB method with a multigrid preconditioner and red-black Gauss-Seidel smoother is used to solve Eq. (55) [75,110,119].

#### 4.4. Structure solver

The structural dynamics, Eqs. (17) and (18), are solved in the following sequence:

$$\mathbf{X}^* = 2\mathbf{X}^n - \mathbf{X}^{n-1}, \quad (56)$$

$$\begin{aligned} \mathcal{D}_s(\mathcal{D}_s(\sigma_i \mathbf{t}^*)) \cdot \mathbf{t}_i^* &= \frac{m_e}{2} \frac{1 - 2(\mathbf{t} \cdot \mathbf{t})_i^n + (\mathbf{t} \cdot \mathbf{t})_i^{n-1}}{\Delta t^2} - m_e (\mathcal{D}_s \mathbf{V} \cdot \mathcal{D}_s \mathbf{V})_i^n \\ &\quad - \mathcal{D}_s(\mathcal{D}_s(\mathbf{q}\mathbf{n})^* - \mathbf{F}_s^n) \cdot \mathbf{t}_i^*, \end{aligned} \quad (57)$$

**Table 2**  
Units of parameters and variables in base units.

Quantity	Unit	Quantity	Unit	Quantity	Unit
$\mathbf{u}$	$LT^{-1}$	$\mathbf{g}$	$LT^{-2}$	$\rho_f$	$ML^{-3}$
$\mu_f$	$ML^{-1}T^{-1}$	$\sigma_{f_1, f_2}$	$MT^{-2}$	$C_{p, f}$	$L^2T^{-2}\Theta^{-1}$
$L_{f_1, f_2}$	$L^2T^{-2}$	$k_f$	$MLT^{-3}\Theta^{-1}$	$m_e$	$ML^{-2}$
$\alpha$	$ML^{-2}T^{-2}$	$\beta$	$ML^{-2}T^{-1}$	$k_b$	$ML^2T^{-2}$
$\mathbf{f}_f$	$ML^{-2}T^{-2}$	$\mathbf{F}_s$	$ML^{1-D_s}T^{-2}$	$\delta(\mathbf{x})$	$L^{-2}$
$q$	$MT^{-2}$	$M$	$MLT^{-2}$	$F_D, F_L$	$MLT^{-2}$
$P$	$ML^2T^{-3}$				

$$m_e \frac{\mathbf{X}_i^{n+1} - \mathbf{X}_i^*}{\Delta t^2} - \left[ \mathcal{D}_s \left( \sigma_i D \mathbf{X}_i^{n+1} \right) + (q\mathbf{n})^{n+1} \right]_i = -\mathbf{F}_s^n, \quad (58)$$

where  $\mathbf{X}^*$  is the predicted position of the fiber at time  $n + 1$  and is used for calculation of all other intermediate variables with superscripts  $*$ , and  $\mathcal{D}_s$  is the difference operator along  $s$ . The tension  $\sigma_i$  is calculated at the intermediate step and is used to update the position of the fiber  $\mathbf{X}_i^{n+1}$ . A similar technique is also employed for the shell structure except that instead of Eq. (57), Eq. (21) is calculated explicitly for the shell based on its dynamics at  $t^n$ . The interaction force between the plate and the fluid,  $\mathbf{F}_s^n$  is evaluated as follows,

$$\mathbf{F}_s^n = -\alpha \sum_{k=1}^n \left[ \mathbf{u}_f^k - \mathbf{u}_s^k \right] \Delta t^k - \beta \left[ \mathbf{u}_f^n - \mathbf{u}_s^n \right]. \quad (59)$$

The fluid velocity along the solid is calculated using a regularized delta function. For the case of the fiber structure, it can be written as:

$$\mathbf{U}_f^n = \sum_{\mathbf{x}} \mathbf{u}^n(\mathbf{x}) \delta_h(\mathbf{x} - \mathbf{X}^n) \Delta x \Delta y, \quad (60)$$

where  $\Delta x$  and  $\Delta y$  are the grid sizes around the solid in  $x$  and  $y$  directions, respectively.  $\delta_h$  is chosen to be a four-point smoothed delta function,

$$\delta_h(\mathbf{x}) = \frac{1}{\Delta x \Delta y} \varphi\left(\frac{x}{\Delta x}\right) \varphi\left(\frac{y}{\Delta y}\right), \quad (61)$$

with

$$\varphi(r) = \begin{cases} 1/8 \left( 3 - 2|r| + \sqrt{1 + 4|r| - 4r^2} \right) & 0 \leq |r| < 1, \\ 1/8 \left( 5 - 2|r| + \sqrt{-7 + 12|r| - 4r^2} \right) & 1 \leq |r| < 2, \\ 0 & 2 \leq |r|. \end{cases} \quad (62)$$

The interpolation method is also extended to the third dimension for the calculations of the shell geometry.

## 5. Numerical tests and applications

To have a consistent algorithmic accuracy, we use the dimensionless parameters and variables in our simulations. We choose the characteristic length ( $L_c$ ), mass ( $M_c$ ), time ( $T_c$ ), and temperature ( $\Theta_c$ ) as the main characteristic quantities, and derive the other characteristic values respectively. The units of the quantities in the system are given in Table 2. There are non-dimensional parameters that can represent the different characteristics of the system and would be helpful for comparison with other studies in the literature:

$$M^* = \frac{\rho_l L_s}{m_e}, \quad U^* = U_\infty L_s \sqrt{\frac{m_e}{k_b}}, \quad Re_l = \frac{\rho_l U_\infty L_s}{\mu_l}, \quad (63)$$

for a structure with a length of  $L_s$  and flow freestream velocity of  $U_\infty$ . The drag force ( $F_D$ ) and lift force ( $F_L$ ) acting on a fiber structure as well as the input power from the flow to the structure ( $P$ ) are calculated from the fluid-structure interaction force density  $\mathbf{F}_s$ ,

$$F_D = - \int_{\Omega_s} \mathbf{F}_s \cdot \mathbf{e}_x ds, \quad F_L = - \int_{\Omega_s} \mathbf{F}_s \cdot \mathbf{e}_y ds, \quad P = \int_{\Omega_s} \mathbf{F}_s \cdot \mathbf{U}_s ds, \quad (64)$$

where  $\mathbf{e}_\chi$  is the unit vector in direction  $\chi$ . A similar relation can be envisioned for the three-dimensional setup.



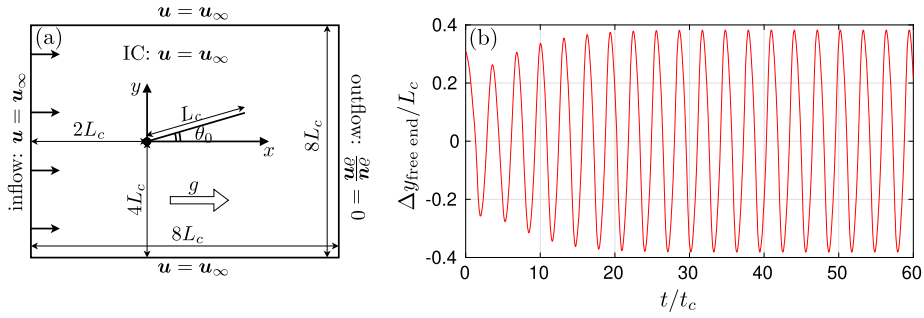


**Fig. 9.** Flexible plate in constant flow test problem. a) Problem domain, initial and boundary conditions. b) Vertical displacement of the plate free end. The limit cycle behavior is consistent after few flaps.

### 5.1. Verification and stability of fluid-structure interaction method

The stability of the overall algorithm depends on not only the stability of the fluid and structural solvers but also the fluid-structure interaction mechanism. For the fluid solver, the main limitation comes from the advection step ( $CFL < 0.5$ ). For the structure solver, an unconditionally stable implicit numerical solver is used. The FSI algorithm here is a feedback method, and the values for the feedback coefficients  $\alpha$  and  $\beta$ , which define the strength of interaction, have effects on the stability of the numerical method. Clearly, for  $\alpha, \beta \rightarrow 0$ , the feedback force goes to zero, and fluid and structure are decoupled. By increasing  $\alpha$  and  $\beta$ , the feedback force becomes large enough to induce an effective penalty mechanism. For large values of  $\alpha$  and  $\beta$ , the calculated force would be too strong, leading to an unstable solution. For selecting the best  $\alpha$  and  $\beta$  values, we follow the approach by Huang and Sung [36], and Shoele and Mittal [105] to set  $\beta = \alpha \Delta t$  and reduce the parameters to one. Also, to have a reasonably distributed structure nodes compared to the fluid grid, we pick  $\Delta s = 0.8 \Delta x$ . Based on the stability analysis of Lee [34] for the temporal integration method, we assume that the model should satisfy a stability criterion with the form

$$C_1 \alpha \Delta t^2 + C_2 \beta \Delta t < C_3, \quad (65)$$

which with the choice of  $\beta = \alpha \Delta t$  reduces to

$$\alpha \Delta t^2 < C_s, \quad (66)$$

where  $C_s$  is a problem specific parameters depends on the problem domain and geometrical setup.

To verify the stability and convergence of the method, we choose a flexible plate pinned on one end and free on the other end in constant incoming flow as a canonical problem and study the dynamic response of the plate and surrounding flow. The problem domain, initial and boundary conditions, shown in Fig. 9.a, are set to match the test case by Huang et al. [36] for a flapping plate with limit cycle dynamics (see Table 8 for parameter values). The displacement of the free end of the plate is shown in Fig. 9.b.

Here, we vary the  $\alpha$  and run the simulation for various  $\Delta s$  and  $\Delta t$  values to check the stability criterion, Eq. (66), using the measured vertical displacement of the free end point. Results are shown in Fig. 10.a (simulations with higher  $\alpha$  values in each case lead to unstable results). The very coarse case with  $\Delta s = L_c/20$  does not show a consistent behavior under increasing  $\alpha$  value, and is unable to capture the correct dynamics. Reducing  $\Delta s$  to  $L_c/40$ ,  $L_c/80$ , and  $L_c/160$  cause convergence under increasing  $\alpha$ , but no consistent critical  $\alpha$  can be found for different space-time resolutions. Scaling the horizontal axis with  $\alpha \Delta t^2$  makes the simulations with the same  $\Delta s$  to have a similar critical  $\alpha \Delta t^2$  stability threshold, but those values are different across different spatial resolutions (see Fig. 10.b). Finally, if  $\alpha$  is combined with spatial and temporal scales as a stability measure  $m_s = \alpha \Delta t^2 / \Delta s$ , a unified value for the stability criterion can be obtained. Based on the simulation results, for this problem,  $m_{s, \text{critical}} \approx 4.2$  (see Fig. 10.c). That is, for  $m_s < m_{s, \text{critical}}$  we expect a convergent solution across different space-time resolutions. This procedure is helpful since one can find the values of  $\alpha$  and  $\beta$  for convergent coarse grid simulations and use the corresponding stability criterion to set  $\alpha$ ,  $\Delta t$ ,  $\Delta s$  values of a convergent solution on finer grid simulations.

The convergence of the method is also tested by refining the spatial and temporal resolution while keeping the value of stability measure constant across simulations,  $\alpha \Delta t^2 / \Delta s = 0.4$ . The results are presented in Table 3, which show a convergence rate of order 0.92 for the amplitude of the free end of the plate using the Richardson extrapolation technique. The comparison of the amplitude and frequency of the finest simulation results show close agreement with the values reported in the literature (see Table 4). The vorticity contours are also shown for four instances in a limit cycle in Fig. 11.

### 5.2. Verification of nucleate pool boiling

The pool boiling is a process in which a superheated substrate is submerged in a pool of liquid, and the boiling phase-change occurs at the interface of the hot substrate and cold liquid. The phase-change process in this method (expect the

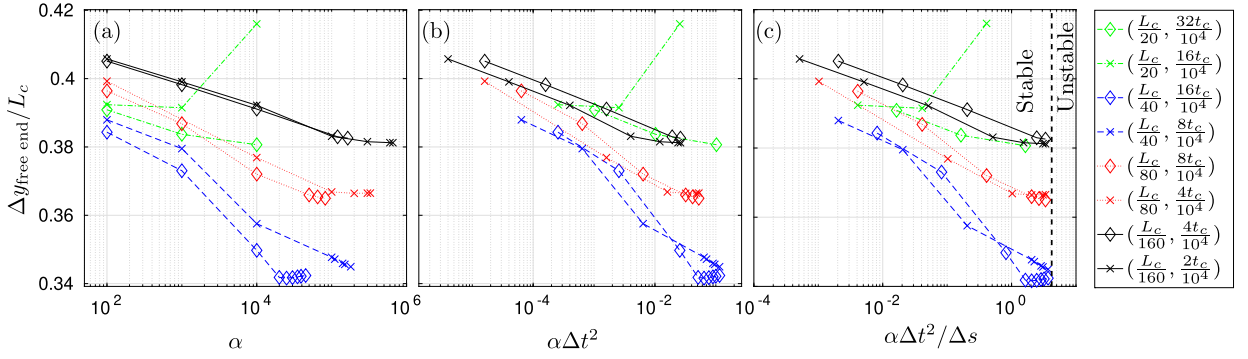


**Fig. 10.** Amplitude of the plate limit cycle under various values of  $(\Delta s, \Delta t)$ . See the online version for the figure in color.

**Table 3**

Simulation parameters for convergence study. The stability measure is constant across the simulation,  $\alpha\Delta t^2/\Delta s = 4.2$ . The amplitude of the free end of the plate converges with  $\mathcal{O}(\Delta x^{0.92})$  under the grid refinement.

$n_x$	$\Delta x$	$n_s$	$\Delta s$	$\Delta t$	$\alpha$	$\Delta y_{\text{free-end}}/L_c$
256	0.03125	40	0.025	0.0016	41015.625	0.3414
512	0.015625	80	0.0125	0.0008	82031.25	0.3675
1024	0.0078125	160	0.00625	0.0004	164062.5	0.3812

**Table 4**

Reported values for dimensionless characteristics of  $\Delta y_{\text{free end}}/L_c$ .

	Amplitude	Frequency
Huang et al. [36]	$\pm 0.35$	0.30
Wang et al. [78]	$\pm 0.35$	0.31
Lee et al. [120]	$\pm 0.38$	0.31
Goza et al. [121]	$\pm 0.38$	0.32
Present	$\pm 0.38$	0.32

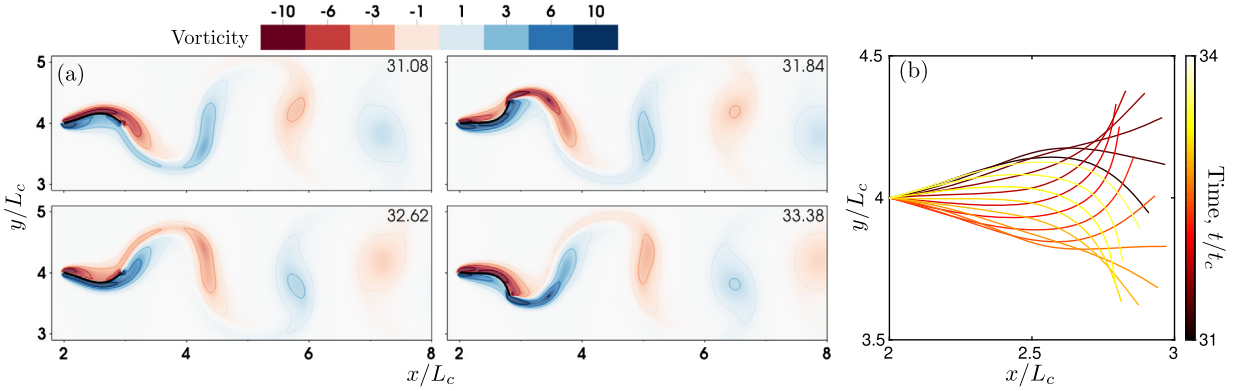


**Fig. 11.** Flexible plate test problem. a) Vorticity contours at times  $t/t_c = 31.08, 31.84, 32.62$  and  $33.38$ . b) Plate position during a one period. See the online version for the figure in color.

micro-model) has been tested and verified based on an analytical solution on a solidification test case [75]. We test the boiling phase-change part of our method with the nucleate pool boiling of a single vapor bubble. The problem initial and boundary conditions are shown in Fig. 12.a for a 2D axisymmetric setup. We choose the parameters to be similar to the experiments reported in [60,113] (see Table 8 for parameter values). The experiment consists of nucleate boiling of water in a test chamber. The substrate is a silicon wafer substrate with a small etched cavity and heated by a copper cylinder around it. The diameter of the vapor bubble in the 2D-axisymmetric simulation shows good agreement with the experimental results. (Fig. 12.b). The similar setup in the 2D-XY simulation shows a significantly longer departure time. This discrepancy is caused by the dimensional suppression of the ratio of buoyancy to surface tension forces in 2D-XY cases.

The diameter of the bubble and the bubble departure times shows convergence under grid refinement in Fig. 12.b. To measure the rate of convergence, the bubble departure times are evaluated in simulations with different resolutions.

**Table 5**

The convergence study of the nucleate pool boiling test. The bubble departure time is evaluated for each simulation and the  $L_1$  norm is used for calculating the error respect to the following finer simulation.

$n_z$	$t_{\text{dep}}/t_c$	Error	Rate
60	3.4623	0.5679	1.0072
120	2.8944	0.2825	0.9654
240	2.6119	0.1447	1.0128
480	2.4672	0.0717	
960	2.3955		

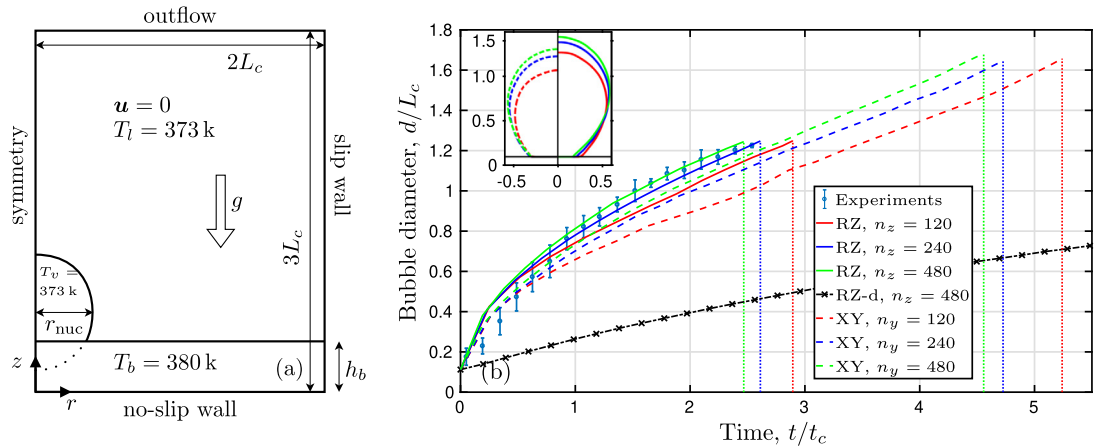


**Fig. 12.** Nucleate boiling verification test. a) Problem domain, initial and boundary conditions. b) Bubble diameter progression from nucleation time. The departure times are shown with the vertical dashed lines. The RZ-d curve (dash-dotted) shows the bubble diameter when micro-model deactivated. Inset: Vapor bubble shape under refinement. Left and right panels show the RZ and XY results respectively at  $T/t_c = 2.3$ . The spatial units are dimensionless with respect to  $L_c$ . See the online version for the figure in color.

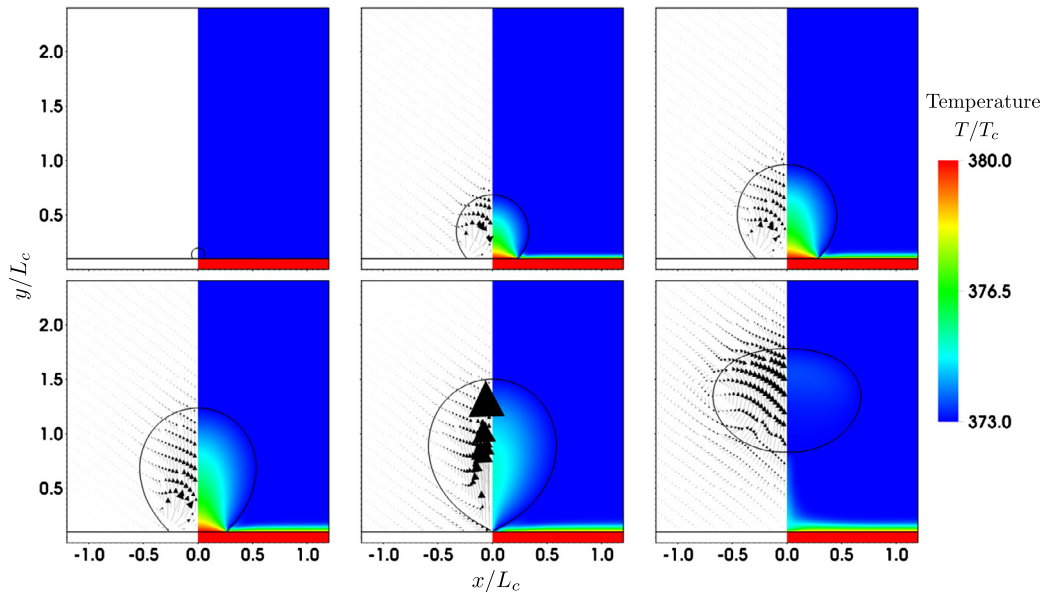


**Fig. 13.** Velocity vector field and temperature for the nucleate boiling test. From left to right and top to bottom, simulation times are  $t/t_c = 0, 0.6, 1.2, 1.8, 2.4, 3.0$ .

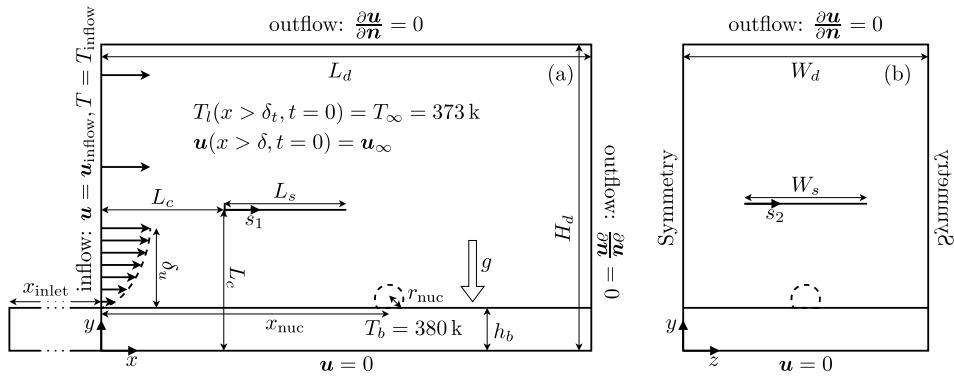


**Fig. 14.** Problem setup, initial conditions, and boundary conditions for the simulation of vortex generator and pool boiling interaction. a) Front view. b) Left view.

The results show a first-order convergence (Table 5). The temperature field and velocity vectors are shown in Fig. 13. To emphasize the significance of the micro-model in the nucleate boiling process, the same test is done with the micro-model deactivated (Fig. 12.b dash-dotted curve). The results show a significant decrease in the bubble growth rate, highlighting the fact that the phase-change models without special treatment of the triple-point region may not be adequate to capture the large temperature gradient at the contact region (where the heat flux become as high as  $10^8$  W/m<sup>2</sup>), and severely underestimate the phase-change rate than the physical value.

### 5.3. Application: pool boiling and vortex generator

The heat flux during the boiling process is usually much higher than the sensible heat flux of the liquid, and some heat exchangers take advantage of this process to achieve higher heat flux capacities. One of the methods to enhance the performance of the heat exchangers is to introduce extra mixing, e.g., by inducing vortices near the heat-exchange interface. Applications of vortex generators are considered in heat exchangers without phase-change [122,123]. Here, we employ the model for the study of active vortex generators in a phase-change process. The test problem consists of vapor bubbles nucleating downstream of a periodically forced plate. The problem setup and initial condition are shown in Fig. 14. The leading edge of the plate is kept parallel to undisturbed incoming flow with respect to the incoming flow and oscillates harmonically perpendicular to the solid interface with  $y_s = L_c + A_s \sin(\frac{2\pi}{t_s}t + \pi)$ , while the free boundary condition is imposed at the trailing edge. We impose hydrodynamic and thermal boundary layer solutions as the initial and inflow boundary conditions. The boundary layer thicknesses at the inflow are calculated for a laminar flow [124]:

$$\delta_u = \sqrt{\frac{\mu_l x_{\text{inlet}}}{\rho_l \mathbf{u}_\infty}}, \quad \delta_T = \frac{\delta_u}{1.026 \sqrt[3]{Pr_l}}, \quad Pr_l = \frac{C_{p,l} \mu_l}{k_l}, \quad (67)$$

where  $x_{\text{inlet}}$  is the distance to the beginning of the flow inlet,  $Pr$  is the Prandtl number, and  $\delta_u, \delta_T$  are hydrodynamics and thermal boundary layer thicknesses. A sample variable of the flow,  $\chi$ , with boundary layer thickness  $\delta_\chi$  has the following profile in the boundary layer transitioning from the bulk value to the value at the surface of the substrate:

$$\frac{\chi(y) - \chi_\infty}{\chi(y=h_b) - \chi_\infty} = 1 - \frac{3}{2} \left( \frac{y-h_b}{\delta_\chi} \right) + \frac{1}{2} \left( \frac{y-h_b}{\delta_\chi} \right)^3 \quad (\text{for } h_b < y < \delta_\chi + h_b), \quad (68)$$

The simulation has an initial period before nucleating vapor bubbles are introduced to the system,  $t < t_{init}$ , to have an appropriate thermal boundary layer development due to the active vortex generation. After the initial time interval, the vapor bubbles are nucleated periodically at the nucleation site at the times  $t_{nuc} = t_{init} + \{0, 1, 2, \dots\} \tau_{nuc}$ .

The convergence of the overall numerical modeling approach is evaluated with this test case in the 2D setup. A setup with smaller domain size ( $L_d/L_c = 4$ ,  $H_d/L_c = 7$ ) and similar parameters given in Table 8 is used for the medium refinement simulation. A single bubble is nucleated at  $t_{\text{nuc}}/t_c = 6$ , and the bubble diameter is evaluated when bubble grows and moves downstream at  $t/t_c = 8$  for three resolutions. The results shows first-order convergence under grid refinement (see Table 6 and Fig. 15).

### 5.3.1. Simulations in 2D

To limit the free parameters in this initial study, we consider four distinct cases of this problem in 2D.

- ▷ No plate: This is the control case. The plate is not included, and only the cross-stream influences the boiling process.
- ▷ Flexible plate: The plate is flexible with constant bending stiffness.
- ▷ Rigid plate: The plate is rigid.

**Table 6**

The convergence study of the pool boiling and vortex generator test case.  $L_1$  norm is used for calculating the error respect to the following finer simulation.

$n_y$	$d_{\text{bubble}}/L_c$	Error	Rate
80	0.9435	0.1914	1.1118
160	1.1349	0.0886	
320	1.2235		

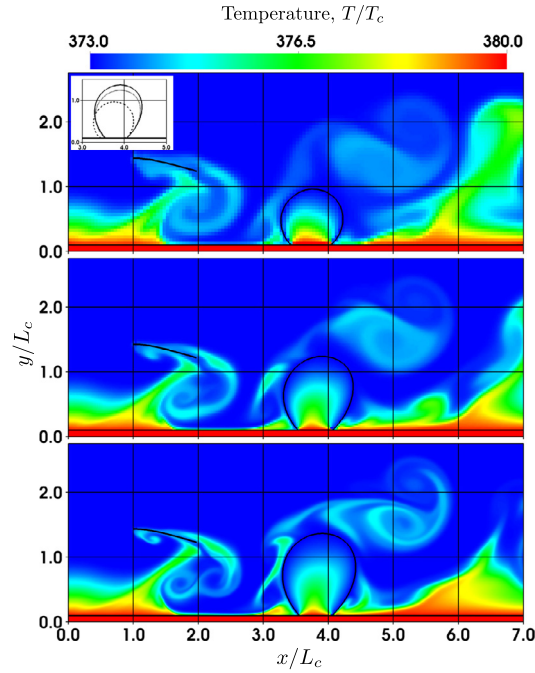


**Fig. 15.** Convergence of the nucleate boiling and vortex generator test simulations under grid refinement. Results are shown at  $t/t_c = 8$ . Inset: overlay of bubble shape for coarse (dashed line), medium (dotted line), and fine (solid line) resolutions.

- Hybrid plate: The first section of the plate that is connected to the oscillating mechanism is rigid, and the second section is flexible. Two different rigid-to-flexible ratios are tested here. The hybrid 25-75 has 25% rigid and 75% flexible parts, and hybrid 50-50 has 50% rigid and 50% flexible parts.

Parameters for the case with the flexible plate are presented in Table 8. We choose the nucleation period to be a multiple of plate forcing period,  $\tau_{\text{nuc}} = 2\tau_s$ . First, we look at the representative bubble diameter and position for the first four nucleated vapor bubbles to check if the system's response is periodic (see Fig. 16). For the cases with no plate, the bubble features (diameter and displacement) are very similar. For the case with the plate included, other than the first bubble, the bubbles grow, move, and detach from the surface similarly. Therefore, we assume that with the periodic movement of the plate (shown in Fig. 17.a), the bubble size and shape would be similar and periodic after the first nucleation for this study. The growth and deformation of the fourth bubbles are shown at several subsequent times frames in Fig. 17.b.

A closer look at the bubble diameter shows that the interaction of the vortex generation and bubbles growth is very minimal. The bubble departure times for the actuated cases are  $\sim 15\%$  longer than the control case, and the bubble sizes at the departure are increased by  $\sim 3\%$ . However, horizontal bubble displacement is more affected by the active vortex generation (see Fig. 18). Compared to the control case, the horizontal bubble displacement at the departure is increased by 40%, 62%, and 60% for the flexible, rigid, and hybrid 50-50 plates, respectively. The extra horizontal displacement of the vapor bubble in cases of the rigid and hybrid plates may be caused by the increased downstream flow created by the downward moving rigid plate and crossflow stream. This modification of the flow streams can also be visible by type of reduction of the thermal boundary layer by the rigid plate compared to the flexible plate case (Fig. 19). For the region just downstream of the plate location ( $2 < x < 7$ ), vortices generated by the rigid plate wash out the thermal boundary more effectively. However, the vortices may bounce off the surface, and have a weaker effect on the regions further downstream. For the flexible plate, the thermal boundary layer is washed off relatively less just downstream of the plate ( $2 < x < 7$ ), but since the vortices are rolling closer to the substrate, they introduce a stronger second wash-out region ( $8 < x < 12$ ). To

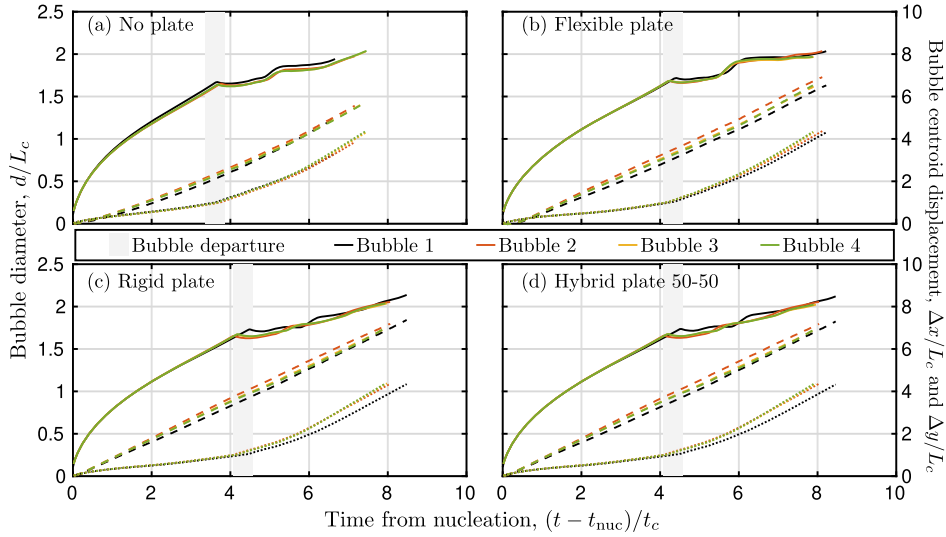


**Fig. 16.** The behavior of the nucleated bubbles after nucleation. The diameter (solid line) is evaluated for a circle with the same circumference. The horizontal displacement (dashed line) and vertical displacement (dotted line) are measured for the centroid position of the bubble. The bubble departure from the surface are shown approximately with the shaded region for each case, and may be pin-pointed by the kink in the bubble diameter curves. The bubbles properties are tracked until any part of them reach  $y = 5L_c$  height. See the online version for the figure in color.

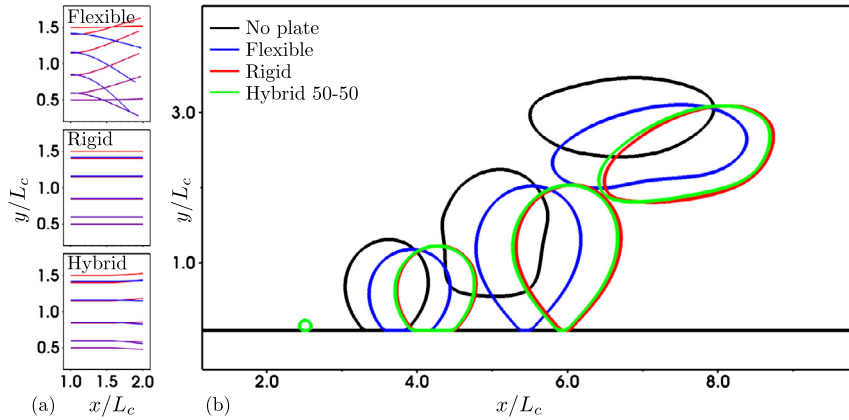


**Fig. 17.** (a) The periodic movement and deformation of the forced flexible, rigid and hybrid 50-50 plates. Each plate is shown at ten frames in their periods with time intervals  $t/t_c = 0.1\tau_s/t_c = 0.3$  (the progress in times is represented with the change of color from red to blue). (b) Nucleation, growth, and departure of the fourth nucleated bubble. The fourth bubble is nucleated at  $t_{nuc}/t_c = 36$  and the bubbles are shown at times  $(t - t_{nuc})/t_c = 0.02, 2, 4$ , and 6. See the online version for the figure in color.

see the differences between two representative cases with flexible and rigid plates, the temperature and velocity values of multiple time frames of each simulation cases are shown in Fig. 20.

The effectiveness of the vortex generation on heat transfer from the substrate to the fluids can be assessed with the convective heat transfer coefficient  $h$  and the average Nusselt number  $Nu$ :

$$h(x) = \frac{-k(\partial T / \partial y)_{y=h_b}}{T_b - T_\infty}, \quad \bar{h} = \frac{1}{L_b} \int_0^{L_b} h(x) dx, \quad Nu = \frac{hL_c}{k}. \quad (69)$$

Fig. 21 shows the Nusselt number of the different simulation cases. Taking the average Nusselt number in the time interval  $t/t_c = [30, 42]$ , where steady periodic values are observed, it is found that the flexible, rigid, hybrid 50-50, and hybrid 25-75 plates increase the Nusselt number to 1.93, 1.98, 2.02, and 2.11 times the control case (no plate actuation). This heat transfer enhancement can also be observed by vortex generation and mixing in the thermal boundary layer. In addition, the vapor bubble growth and its interaction with the plate enhance the mixing and heat transfer further (see Fig. 20).

Another aspect of this system is a fluid-structure force acting on the plate and surrounding flow. We evaluate the drag and lift forces and the corresponding power of the plate in each simulation case (see Fig. 22). The average values of these



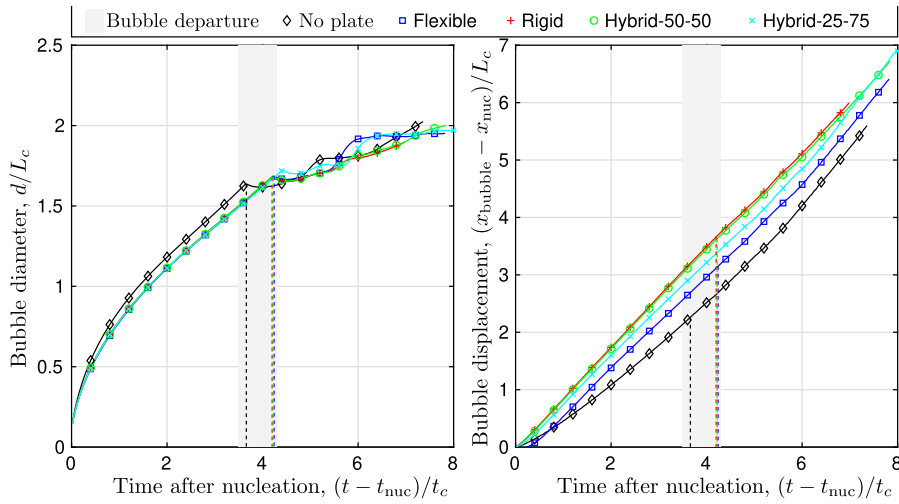


**Fig. 18.** The diameter and horizontal displacement of fourth vapor bubble. The bubble departure time from the substrate is marked with the dashed lines.

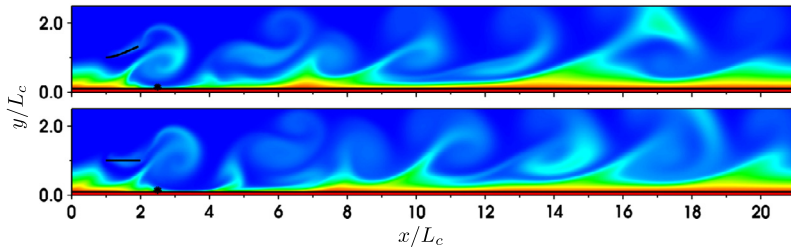


**Fig. 19.** The temperature profile near the hot substrate at  $t/t_c = 18$ . This figure has the same color table as Fig. 20 for temperature.

**Table 7**

The average value of drag and lift forces, and power of the plate in the time interval  $t/t_c = [36, 42]$ .

Case	Rigid %	Flexible %	$\overline{Nu}$	$\overline{F_D}/F_c$	$\overline{(F_L)_{RMS}}/F_c$	$\overline{P}/P_c$	COE
Control			2.107				
Rigid	100%	0%	4.166	0.019	2.659	1.726	1.193
Hybrid 50-50	50%	50%	4.252	-0.015	2.626	1.758	1.220
Hybrid 25-75	25%	75%	4.451	-0.149	2.531	1.842	1.273
Flexible	0%	100%	4.071	-0.278	1.816	1.389	1.413

measurements in the time interval  $t/t_c = [36, 42]$  are presented in Table 7. The rigid case introduces the most amount of drag. For the other cases, the generated thrust is decreasing with the reduction of the rigid section of the plate. The RMS value of the lift force as well decreases with the percentage of the rigid part of the plate. Comparing the power necessary to induce the prescribed motion to the plates, the flexible plate shows the least amount of power consumption. One can combine the measurements for the enhanced heat transfer due to active vortex generation to the power consumption of the plate to evaluate a coefficient of the performance  $COE = (Nu - Nu_{control})/(\overline{P}/P_c)$ . The COE of the flexible plate is  $\sim 18\%$  higher than the rigid and hybrid plates (see Table 7). This brief analysis shows that the introduction of active vortex generators enhances thermal heat transfer. A rigid plate may be used to push the vapor bubbles away from the nucleation site and subsequently avoid the transition from nucleate boiling to film boiling and increase the critical heat flux of the boiling process. The flexible plate, on the other hand, needs less actuation energy and is the more efficient heat transfer case for similar input power.

### 5.3.2. Simulations in 3D

As mentioned in subsection 5.2, the 2D XY model of the boiling process may result in an overestimated departure time due to the changes in the ratio of the buoyancy to surface tension forces. The 2D simulations of the boiling process are useful to find the effective variables and their roles in the performance of the system. A 3D simulation would be more realistic and shows the capability of the current method to capture the physical responses of the combined phase-change



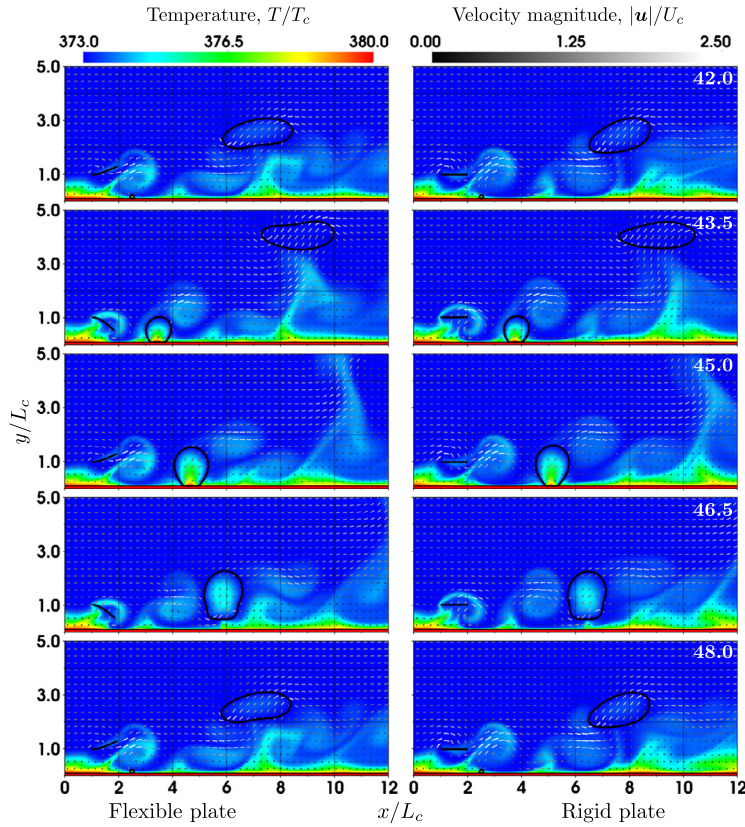


**Fig. 20.** The temperature and velocity evolution of the system around and downstream of the nucleation site. The timestamps are dimensionless in respect to  $t_c$ .

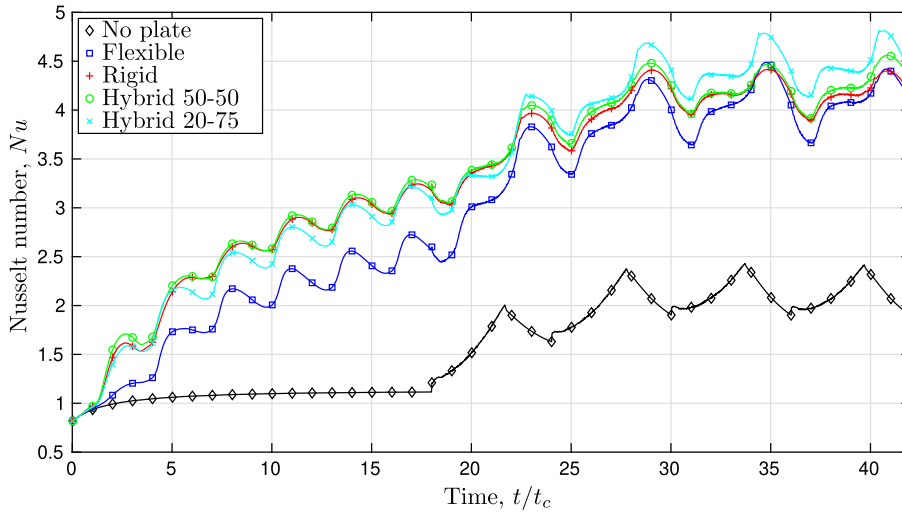


**Fig. 21.** Nusselt number in the boiling and vortex generator simulations.

and FSI system. Here, we present the results for the 3D simulation of the active vortex generator using a shell structure as a flexible plate. Fig. 23.a shows the isosurface of the Q-criterion and the way vortices are created from the free boundaries of the plate and transport the bubble further downstream. It is noticeable that this behavior is, to some extent, narrow and depends on the width of the plate in this simulation, which can also be seen from the streamwise temperature cross-sections. The reduction of the thermal boundary layer at the center of the plate (Fig. 23.b) and the outer ridge of the plate (Fig. 23.c) are qualitatively similar to the 2D results. However, the temperature away from the centerline, where it is not

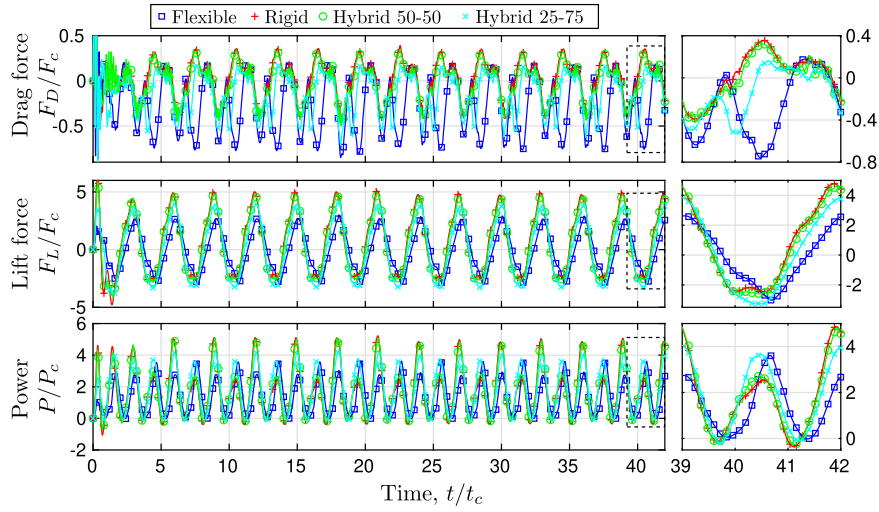


**Fig. 22.** The drag force, lift force, and power of the structure in the boiling and vortex generator simulations. The expanded views of the dashed rectangle are shown on the corresponding plots in the right column.

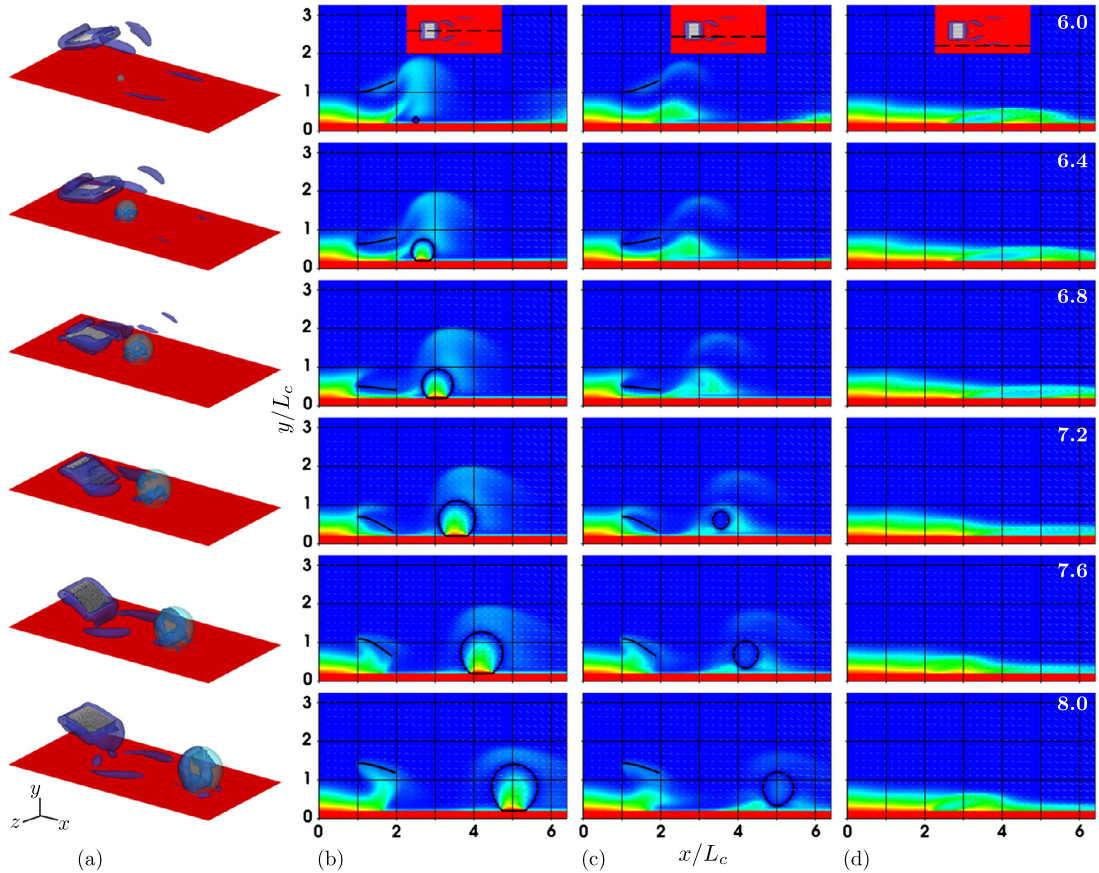


**Fig. 23.** 3D simulation results of active vortex generation and nucleate pool boiling. (a) Isosurface of  $Q_{\text{criterion}} = 4$ . Temperature cross section profiles at (b)  $z/L_c = 0$ , (c)  $z/L_c = 0.5$ , and (d)  $z/L_c = 1$  from the centerline of the domain in  $z$  direction. The cross-section locations are also shown in the top-view insets in the first row. The bubble is nucleated at  $t_{\text{init}}/t_c = 6$ . The dimensionless time of each frame shown in the right column of each row. The similar color tables are used as in Fig. 20.

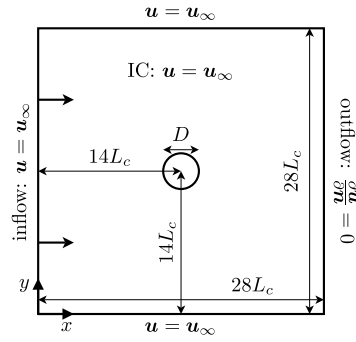


Fig. 24. Problem setup for the flow around a rigid stationary cylinder verification test.

directly downstream of the plate, shows less reduction in the thermal boundary layer (Fig. 23.d). Therefore, it is critical to locate the position of an active vortex generator near the potential nucleation sites to achieve an effective modification of bubble dynamics and local modification of the thermal boundary layer.

## 6. Conclusion

We have presented a modeling and simulation approach for multi-material/multi-phase systems, which also include fluid-structure interaction for flexible geometries such as fibers and shells in two and three dimensions. The use of continuous moment-of-fluid reconstruction method makes this approach capable of handling problems with significant surface tension forces with accurate and robust interface representation and evolution. The phase-change algorithm and specifically the micro-region model, along with the proposed fluid-structure interaction method, gave us the ability to look at the interaction of active vortex generation and nucleate pool boiling. The initial results show that the active vortex generation may be used for enhancing the heat transfer in one-phase and two-phase systems, and manipulate the bubble dynamics in a crossflow.

Although the initial simulations show promising results, this system is fairly unknown at this point. Further studies are needed to understand the system dynamics better and accurately analyze the effect of extensive parameter domain related to material and fluid properties on the flow regimes, thermal dynamics, and efficiency of the system. The setup using the fiber structure is beneficial for parameter study and fast simulations. The shell structure and the 3D setup will be used to explore dynamics of the system such as the plate size ratio  $W/L$  and edge effects. Following a similar approach for fluid-structure interaction, using a structure solver for volumetric geometries, more general systems will be studied for phase-change induced heat transfer.

The general scope of this computational approach enables us to explore other physical problems with significant interfacial dynamics (phase-change, surface-tension, and fluid-structure interaction) with minimal effort for problem setup.

## CRediT authorship contribution statement

**Mehdi Vahab:** Conceptualization, Software, Methodology, Writing, Validation. **Mark Sussman:** Software, Methodology, Validation. **Kourosh Shoele:** Conceptualization, Supervision, Methodology, Writing, Validation, Supervision.

## Declaration of competing interest

The authors declare that they have no known competing financial interests or personal relationships that could have appeared to influence the work reported in this paper.

## Appendix A. Flow around a rigid stationary cylinder

We show a fluid-structure interaction test with a rigid, static body here as well. A circular cylinder is put in the constant incoming flow. The problem setup is shown in Fig. 24. The following characteristic values are set based on the velocity and density at the inflow ( $U_c = U_\infty = 1$  m/s,  $\rho_c = \rho_\infty = 1$  kg/m<sup>3</sup>), and the diameter of the cylinder ( $L_c = D = 1$  m). The fluid and structure domains are discretized by a  $1680 \times 1680$  and 180 equidistant grids respectively. For the test, we used  $\Delta t/t_c = 10^{-3}$ ,  $\alpha = 100$ , and  $\beta = 0.1$ , and inflow with  $Re = \rho_l U_\infty D / \mu_l = 100$ . After some transient time, a stable vortex shedding regime is observed behinds the cylinder. The induced lift and drag forces on the cylinder are measured and corresponding coefficients are calculated (see Fig. 25). There is a good agreement between results of present study and value reported in the literature (see Table 9).

**Table 8**

Parameter values for the test problems. The value on the lower part of the tables are dimensionless.

Variable	Unit in base units	FSI-flag verification	Pool boiling RZ (XY) verification	Pool boiling and oscillating plate 2D (3D)
$L_c$	L	1 m	$2.2391 \times 10^{-3}$ m	$2.2391 \times 10^{-3}$ m
$t_c$	T	1 s	$1.512 \times 10^{-2}$ s	$1.512 \times 10^{-2}$ s
$M_c$	M	1 kg	$1.705 \times 10^{-5}$ kg	$1.705 \times 10^{-5}$ kg
$T_c$	$\Theta$	Same as K	Same as K	Same as K
$\rho_c$	$ML^{-3}$	$1 \text{ kg/m}^3$	$9.580 \times 10^2 \text{ kg/m}^3$	$9.580 \times 10^3 \text{ kg/m}^3$
$U_c$	$LT^{-1}$	1 m/s	$1.481 \times 10^{-1}$ m/s	$1.481 \times 10^{-1}$ m/s
$L_d$	L	8	2 (4)	21 (6.4)
$H_d$	L	8	3	6 (6.4)
$W_d$	L			(3.2)
$n_x$ or $n_r$		512	320 (640)	840 (128)
$n_y$		512	480	240 (128)
$n_z$			(480)	(64)
$n_s$		64		50, (25 $\times$ 25)
$\Delta t$	T	$2 \times 10^{-3}$	CFL = 0.5	$4 \times 10^{-4}$ (2 $\times 10^{-4}$ )
$U_\infty$ or $\bar{U}$	$LT^{-1}$	1		1
$ g $	$LT^{-2}$	0.5	1	1
$\alpha$	$ML^{-2}T^{-2}$	$10^5$		$10^2$ ( $10^3$ )
$\beta$	$ML^{-2}T^{-1}$	$10^2$		$10^{-2}$ ( $10^1$ )
$m_e$	$ML^{-2}$	1.5		0.2
$k_b$	$ML^2T^{-2}$	$10^{-3}$		0.5946
$\phi_{11}, \phi_{22}, \phi_{12}$				(1000, 1000, 10)
$M^*$		2/3		4.998
$U^*$		$3.87 \times 10^{-2}$		$5.801 \times 10^{-1}$
$\rho_l$	$ML^{-3}$	1	1	1
$\rho_v$	$ML^{-3}$		$6.217 \times 10^{-4}$	$6.217 \times 10^{-4}$
$\mu_l$	$ML^{-1}T^{-1}$	$5 \times 10^{-3}$	$8.780 \times 10^{-4}$	$8.780 \times 10^{-3}$
$\mu_v$	$ML^{-1}T^{-1}$		$3.783 \times 10^{-5}$	$3.783 \times 10^{-4}$
$\sigma_{lv}$	$MT^{-2}$		$9.994 \times 10^{-1}$	$9.994 \times 10^{-1}$
$\sigma_{ls}$	$MT^{-2}$		$9.444 \times 10^{-1}$	$9.444 \times 10^{-1}$
$\sigma_{vs}$	$MT^{-2}$		1.587	1.587
$\theta$			50	50
$C_{p,l}$	$L^2T^{-2}\Theta^{-1}$		$1.921 \times 10^5$	$4.217 \times 10^5$
$C_{p,v}$	$L^2T^{-2}\Theta^{-1}$		$9.247 \times 10^4$	$2.029 \times 10^5$
$L_{l,v}$	$L^2T^{-2}$		$1.029 \times 10^8$	$1.029 \times 10^8$
$k_l$	$MLT^{-3}\Theta^{-1}$		$9.752 \times 10^1$	$9.751 \times 10^1$
$k_v$	$MLT^{-3}\Theta^{-1}$		3.559	3.559
$R_{nuc}$	L		0.06	0.06 (0.12)
$x_{nuc}$	L		0	2.5
$\tau_{nuc}$	T			6
$t_{init}$	T		0	18 (6)
$h_b$	L		0.1	0.1 (0.2)
$h_{mic}$	L		$4.4661 \times 10^{-9}$	$4.4661 \times 10^{-9}$
$h_{mac}$	L		$5.000 \times 10^{-2}$	$5.000 \times 10^{-2}$
$\theta_{mic}$			50	50
$x_{inlet}$	L			150
$\delta_u$	L			1.125
$\delta_T$	L		0	$9.136 \times 10^{-1}$
$A_s$	L			0.5
$\tau_s$	T			3
$Re$		$2 \times 10^2$		$1.139 \times 10^3$

**Table 9**

The lift and drag coefficients for the flow around a rigid stationary cylinder verification test.

	$\bar{C}_D$	$C_L^{(1)}$
Lai et al. [35]	1.46	0.33
Shin et al. [37]	1.36	0.33
Shoele et al. [80]	1.35	0.33
Present	1.39	0.32

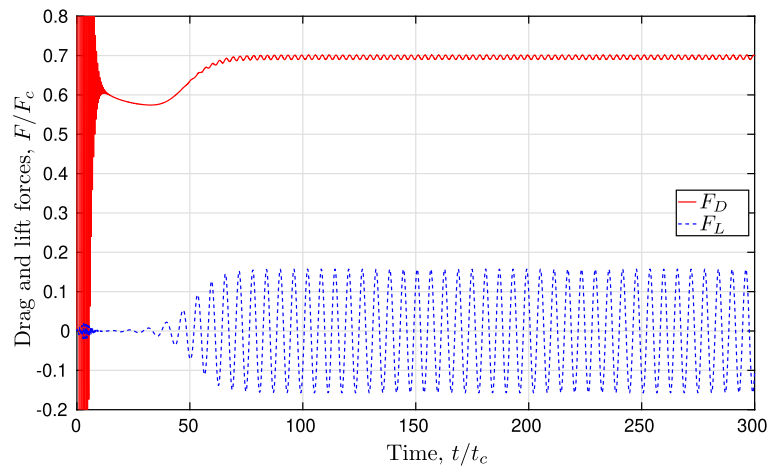


Fig. 25. The drag and lift forces for the flow around a rigid stationary cylinder verification test.

## References

- [1] A. Faghri, Review and advances in heat pipe science and technology, *J. Heat Transf.* 134 (12) (2012) 123001.
- [2] X. Chen, H. Ye, X. Fan, T. Ren, G. Zhang, A review of small heat pipes for electronics, *Appl. Therm. Eng.* 96 (2016) 1–17.
- [3] L.J. Hastings, D. Plachta, L. Salerno, P. Kittel, An overview of NASA efforts on zero boiloff storage of cryogenic propellants, *Cryogenics* 41 (11–12) (2001) 833–839.
- [4] C. Muratov, V.V. Osipov, V.N. Smelyanskiy, Issues of long-term cryogenic propellant storage in microgravity, Tech. Rep. 20120011680, NASA Ames Research Center, Moffett Field, CA, United States, 2011.
- [5] R. Scardovelli, S. Zaleski, Direct numerical simulation of free-surface and interfacial flow, *Annu. Rev. Fluid Mech.* 31 (1) (1999) 567–603.
- [6] G. Tryggvason, R. Scardovelli, S. Zaleski, *Direct Numerical Simulations of Gas–Liquid Multiphase Flows*, Cambridge University Press, 2011.
- [7] J.M. Hyman, Numerical methods for tracking interfaces, *Physica D* 12 (1–3) (1984) 396–407.
- [8] S. Osher, J.A. Sethian, Fronts propagating with curvature-dependent speed: algorithms based on Hamilton–Jacobi formulations, *J. Comput. Phys.* 79 (1) (1988) 12–49.
- [9] C.W. Hirt, B.D. Nichols, Volume of fluid (VOF) method for the dynamics of free boundaries, *J. Comput. Phys.* 39 (1) (1981) 201–225.
- [10] V. Dyadechko, M. Shashkov, Moment-of-fluid interface reconstruction, Los Alamos Report LA-UR-05-7571.
- [11] W.F. Noh, P. Woodward, Slic (simple line interface calculation), in: *Proceedings of the Fifth International Conference on Numerical Methods in Fluid Dynamics*, June 28–July 2, 1976, Twente University, Enschede, Springer, 1976, pp. 330–340.
- [12] W.J. Rider, D.B. Kothe, Reconstructing volume tracking, *J. Comput. Phys.* 141 (2) (1998) 112–152.
- [13] E. Puckett, J. Saltzman, A 3d adaptive mesh refinement algorithm for multimaterial gas dynamics, *Physica D* 60 (1–4) (1992) 84–93.
- [14] N. Ashgriz, J. Poo, Flair: flux line-segment model for advection and interface reconstruction, *J. Comput. Phys.* 93 (2) (1991) 449–468.
- [15] D.L. Youngs, Time-dependent multi-material flow with large fluid distortion, in: *Numerical Methods for Fluid Dynamics*, 1982, pp. 273–285.
- [16] E.G. Puckett, A volume-of-fluid interface tracking algorithm with applications to computing shock wave refraction, in: *Proceedings of the Fourth International Symposium on Computational Fluid Dynamics*, 1991, pp. 933–938.
- [17] J.E. Pilliod Jr, E.G. Puckett, Second-order accurate volume-of-fluid algorithms for tracking material interfaces, *J. Comput. Phys.* 199 (2) (2004) 465–502.
- [18] V. Dyadechko, M. Shashkov, Reconstruction of multi-material interfaces from moment data, *J. Comput. Phys.* 227 (11) (2008) 5361–5384.
- [19] S.P. Schofield, R.V. Garimella, M.M. Francois, R. Loubère, Material order-independent interface reconstruction using power diagrams, *Int. J. Numer. Methods Fluids* 56 (6) (2008) 643–659.
- [20] S.P. Schofield, R.V. Garimella, M.M. Francois, R. Loubère, A second-order accurate material-order-independent interface reconstruction technique for multi-material flow simulations, *J. Comput. Phys.* 228 (3) (2009) 731–745.
- [21] A. Pathak, M. Raessi, A three-dimensional volume-of-fluid method for reconstructing and advecting three-material interfaces forming contact lines, *J. Comput. Phys.* 307 (2016) 550–573.
- [22] G. Hou, J. Wang, A. Layton, Numerical methods for fluid–structure interaction – a review, *Commun. Comput. Phys.* 12 (2) (2012) 337–377.
- [23] E.H. Dowell, K.C. Hall, Modeling of fluid–structure interaction, *Annu. Rev. Fluid Mech.* 33 (1) (2001) 445–490.
- [24] C.S. Peskin, Numerical analysis of blood flow in the heart, *J. Comput. Phys.* 25 (3) (1977) 220–252.
- [25] C.S. Peskin, The immersed boundary method, *Acta Numer.* 11 (2002) 479–517.
- [26] C.S. Peskin, The fluid dynamics of heart valves: experimental, theoretical, and computational methods, *Annu. Rev. Fluid Mech.* 14 (1) (1982) 235–259.
- [27] R.P. Beyer, R.J. LeVeque, Analysis of a one-dimensional model for the immersed boundary method, *SIAM J. Numer. Anal.* 29 (2) (1992) 332–364.
- [28] R. Verzicco, J. Mohd-Yusof, P. Orlandi, D. Haworth, LES in complex geometries using boundary body forces, in: *Center for Turbulence Research Proceedings of the Summer Program*, NASA Ames and Stanford University, 1998, pp. 171–186.
- [29] E. Balaras, Modeling complex boundaries using an external force field on fixed Cartesian grids in large-eddy simulations, *Comput. Fluids* 33 (3) (2004) 375–404.
- [30] G. Iaccarino, R. Verzicco, Immersed boundary technique for turbulent flow simulations, *Appl. Mech. Rev.* 56 (3) (2003) 331–347.
- [31] K. Taira, T. Colonius, The immersed boundary method: a projection approach, *J. Comput. Phys.* 225 (2) (2007) 2118–2137.
- [32] D. Goldstein, R. Handler, L. Sirovich, Modeling a no-slip flow boundary with an external force field, *J. Comput. Phys.* 105 (2) (1993) 354–366.
- [33] E. Saiki, S. Biringen, Numerical simulation of a cylinder in uniform flow: application of a virtual boundary method, *J. Comput. Phys.* 123 (2) (1996) 450–465.
- [34] C. Lee, Stability characteristics of the virtual boundary method in three-dimensional applications, *J. Comput. Phys.* 184 (2) (2003) 559–591.
- [35] M.-C. Lai, C.S. Peskin, An immersed boundary method with formal second-order accuracy and reduced numerical viscosity, *J. Comput. Phys.* 160 (2) (2000) 705–719.
- [36] W.-X. Huang, S.J. Shin, H.J. Sung, Simulation of flexible filaments in a uniform flow by the immersed boundary method, *J. Comput. Phys.* 226 (2) (2007) 2206–2228.



- [37] S.J. Shin, W.-X. Huang, H.J. Sung, Assessment of regularized delta functions and feedback forcing schemes for an immersed boundary method, *Int. J. Numer. Methods Fluids* 58 (3) (2008) 263–286.
- [38] R. Mittal, G. Iaccarino, Immersed boundary methods, *Annu. Rev. Fluid Mech.* 37 (2005) 239–261.
- [39] B.E. Griffith, N.A. Patankar, Immersed methods for fluid–structure interaction, *Annu. Rev. Fluid Mech.* 52 (2019) 421–448.
- [40] V. Voller, M. Cross, Accurate solutions of moving boundary problems using the enthalpy method, *Int. J. Heat Mass Transf.* 24 (3) (1981) 545–556.
- [41] V. Voller, Implicit finite difference solutions of the enthalpy formulation of Stefan problems, *IMA J. Numer. Anal.* 5 (2) (1985) 201–214.
- [42] Y. Cao, A. Faghri, W.S. Chang, A numerical analysis of Stefan problems for generalized multi-dimensional phase-change structures using the enthalpy transforming model, *Int. J. Heat Mass Transf.* 32 (7) (1989) 1289–1298.
- [43] G. Chaudhary, R. Li, Freezing of water droplets on solid surfaces: an experimental and numerical study, *Exp. Therm. Fluid Sci.* 57 (2014) 86–93.
- [44] S. Tabakova, F. Feuillebois, S. Radev, Freezing of a supercooled spherical droplet with mixed boundary conditions, *Proc. R. Soc. Lond., Ser. A, Math. Phys. Eng. Sci.* 466 (2010) 1117–1134.
- [45] S. Alavi, M. Passandideh-Fard, J. Mostaghimi, Simulation of semi-molten particle impacts including heat transfer and phase change, *J. Therm. Spray Technol.* 21 (6) (2012) 1278–1293.
- [46] H. Li, P. Wang, L. Qi, H. Zuo, S. Zhong, X. Hou, 3d numerical simulation of successive deposition of uniform molten al droplets on a moving substrate and experimental validation, *Comput. Mater. Sci.* 65 (2012) 291–301.
- [47] M. Pasandideh-Fard, S. Chandra, J. Mostaghimi, A three-dimensional model of droplet impact and solidification, *Int. J. Heat Mass Transf.* 45 (11) (2002) 2229–2242.
- [48] M. Raessi, M. Thiele, B. Amirzadeh, Computational simulation of the impact and freezing of micron-size water droplets on super-hydrophobic surfaces, in: *ASME 2013 Heat Transfer Summer Conference Collocated with the ASME 2013 7th International Conference on Energy Sustainability and the ASME 2013 11th International Conference on Fuel Cell Science, Engineering and Technology*, American Society of Mechanical Engineers, 2013, V002T07A032.
- [49] F. Gibou, L. Chen, D. Nguyen, S. Banerjee, A level set based sharp interface method for the multiphase incompressible Navier–Stokes equations with phase change, *J. Comput. Phys.* 222 (2) (2007) 536–555.
- [50] S. Shin, D. Juric, Modeling three-dimensional multiphase flow using a level contour reconstruction method for front tracking without connectivity, *J. Comput. Phys.* 180 (2) (2002) 427–470.
- [51] D. Juric, G. Tryggvason, Computations of boiling flows, *Int. J. Multiph. Flow* 24 (3) (1998) 387–410.
- [52] R.W. Schrage, *A Theoretical Study of Interphase Mass Transfer*, Columbia University Press, 1953.
- [53] C. Kunkelmann, P. Stephan, Cfd simulation of boiling flows using the volume-of-fluid method within openfoam, *Numer. Heat Transf., Part A, Appl.* 56 (8) (2009) 631–646.
- [54] S. Shin, B. Choi, Numerical simulation of a rising bubble with phase change, *Appl. Therm. Eng.* 100 (2016) 256–266.
- [55] G. Son, V. Dhir, Numerical simulation of film boiling near critical pressures with a level set method, *J. Heat Transf.* 120 (1) (1998) 183–192.
- [56] R. Marek, J. Straub, Analysis of the evaporation coefficient and the condensation coefficient of water, *Int. J. Heat Mass Transf.* 44 (1) (2001) 39–53.
- [57] J. Rose, On interphase matter transfer, the condensation coefficient and dropwise condensation, *Proc. R. Soc. Lond. Ser. A, Math. Phys. Sci.* 411 (1841) (1987) 305–311.
- [58] W. Lee, A pressure iteration scheme for two-phase flow modeling, in: *Multiphase Transport Fundamentals, Reactor Safety, Applications*, Hemisphere Publishing, Washington, DC, 1980, pp. 407–431.
- [59] L.R. Villegas, R. Alis, M. Lepilliez, S. Tanguy, A ghost fluid/level set method for boiling flows and liquid evaporation: application to the Leidenfrost effect, *J. Comput. Phys.* 316 (2016) 789–813.
- [60] G. Son, V. Dhir, N. Ramanujapu, Dynamics and heat transfer associated with a single bubble during nucleate boiling on a horizontal surface, *J. Heat Transf.* 121 (3) (1999) 623–631.
- [61] J. Kern, P. Stephan, et al., Theoretical model for nucleate boiling heat and mass transfer of binary mixtures, *J. Heat Transf.* 125 (6) (2003) 1106–1115.
- [62] Y. Sato, B. Niceno, Nucleate pool boiling simulations using the interface tracking method: boiling regime from discrete bubble to vapor mushroom region, *Int. J. Heat Mass Transf.* 105 (2017) 505–524.
- [63] A. Urbano, S. Tanguy, G. Huber, C. Colin, Direct numerical simulation of nucleate boiling in micro-layer regime, *Int. J. Heat Mass Transf.* 123 (2018) 1128–1137.
- [64] C.R. Kharangate, I. Mudawar, Review of computational studies on boiling and condensation, *Int. J. Heat Mass Transf.* 108 (2017) 1164–1196.
- [65] A. Esmaeeli, G. Tryggvason, Computations of film boiling. Part I: numerical method, *Int. J. Heat Mass Transf.* 47 (25) (2004) 5451–5461.
- [66] M. Yuan, Y. Yang, T. Li, Z. Hu, Numerical simulation of film boiling on a sphere with a volume of fluid interface tracking method, *Int. J. Heat Mass Transf.* 51 (7–8) (2008) 1646–1657.
- [67] G. Tryggvason, B. Bunner, A. Esmaeeli, D. Juric, N. Al-Rawahi, W. Tauber, J. Han, S. Nas, Y.-J. Jan, A front-tracking method for the computations of multiphase flow, *J. Comput. Phys.* 169 (2) (2001) 708–759.
- [68] H. Luo, J.D. Baum, R. Löhner, On the computation of multi-material flows using ale formulation, *J. Comput. Phys.* 194 (1) (2004) 304–328.
- [69] A. Caboussat, M.M. Francois, R. Glowinski, D.B. Kothe, J.M. Scialian, A numerical method for interface reconstruction of triple points within a volume tracking algorithm, *Math. Comput. Model.* 48 (11) (2008) 1957–1971.
- [70] C. Sijoy, S. Chaturvedi, Volume-of-fluid algorithm with different modified dynamic material ordering methods and their comparisons, *J. Comput. Phys.* 229 (10) (2010) 3848–3863.
- [71] M. Kucharik, R.V. Garimella, S.P. Schofield, M.J. Shashkov, A comparative study of interface reconstruction methods for multi-material ale simulations, *J. Comput. Phys.* 229 (7) (2010) 2432–2452.
- [72] D.P. Starinshak, S. Karni, P.L. Roe, A new level set model for multimaterial flows, *J. Comput. Phys.* 262 (2014) 1–16.
- [73] T.V. Vu, G. Tryggvason, S. Homma, J.C. Wells, Numerical investigations of drop solidification on a cold plate in the presence of volume change, *Int. J. Multiph. Flow* 76 (2015) 73–85.
- [74] A. Esmaeeli, G. Tryggvason, A front tracking method for computations of boiling in complex geometries, *Int. J. Multiph. Flow* 7 (30) (2004) 1037–1050.
- [75] M. Vahab, C. Pei, M.Y. Hussaini, M. Sussman, Y. Lian, An adaptive coupled level set and moment-of-fluid method for simulating droplet impact and solidification on solid surfaces with application to aircraft icing, in: *54th AIAA Aerospace Sciences Meeting*, 2016, p. 1340.
- [76] M. Uhlmann, An immersed boundary method with direct forcing for the simulation of particulate flows, *J. Comput. Phys.* 209 (2) (2005) 448–476.
- [77] L. Wang, G.M. Currao, F. Han, A.J. Neely, J. Young, F.-B. Tian, An immersed boundary method for fluid–structure interaction with compressible multi-phase flows, *J. Comput. Phys.* 346 (2017) 131–151.
- [78] K. Wang, P. Lea, C. Farhat, A computational framework for the simulation of high-speed multi-material fluid–structure interaction problems with dynamic fracture, *Int. J. Numer. Methods Eng.* 104 (7) (2015) 585–623.
- [79] L. Yang, A.J. Gil, A.A. Carreño, J. Bonet, Unified one-fluid formulation for incompressible flexible solids and multiphase flows: application to hydrodynamics using the immersed structural potential method (ispm), *Int. J. Numer. Methods Fluids* 86 (1) (2018) 78–106.
- [80] K. Shoele, Q. Zhu, Leading edge strengthening and the propulsion performance of flexible ray fins, *J. Fluid Mech.* 693 (2012) 402–432.
- [81] K. Shoele, Q. Zhu, Performance of a wing with nonuniform flexibility in hovering flight, *Phys. Fluids* 25 (4) (2013) 041901.
- [82] K. Shoele, R. Mittal, Computational study of flow-induced vibration of a reed in a channel and effect on convective heat transfer, *Phys. Fluids* 26 (12) (2014) 127103.

- [83] J.B. Lee, S.G. Park, B. Kim, J. Ryu, H.J. Sung, Heat transfer enhancement by flexible flags clamped vertically in a Poiseuille channel flow, *Int. J. Heat Mass Transf.* 107 (2017) 391–402.
- [84] L. Tang, M.P. Paidoussis, J. Jiang, Cantilevered flexible plates in axial flow: energy transfer and the concept of Flutter-Mill, *J. Sound Vib.* 326 (1–2) (2009) 263–276.
- [85] F. Invernizzi, S. Dulio, M. Patrini, G. Guizzetti, P. Mustarelli, Energy harvesting from human motion: materials and techniques, *Chem. Soc. Rev.* 45 (20) (2016) 5455–5473.
- [86] A. Dewan, P. Mahanta, K.S. Raju, P.S. Kumar, Review of passive heat transfer augmentation techniques, *Proc. Inst. Mech. Eng. A, J. Power Energy* 218 (7) (2004) 509–527.
- [87] T. Crittenden, S. Jha, A. Glezer, Forced convection heat transfer enhancement in heat sink channels using aeroelastically fluttering reeds, in: 2017 16th IEEE Intersociety Conference on Thermal and Thermomechanical Phenomena in Electronic Systems, ITherm, IEEE, 2017, pp. 114–121.
- [88] Y. Yu, Y. Liu, Y. Chen, Vortex dynamics and heat transfer behind self-oscillating inverted flags of various lengths in channel flow, *Phys. Fluids* 30 (4) (2018) 045104.
- [89] Z. Anxionnaz, M. Cabassud, C. Gourdon, P. Tochon, Heat exchanger/reactors (hex reactors): concepts, technologies: state-of-the-art, *Chem. Eng. Process. Process. Intensif.* 47 (12) (2008) 2029–2050.
- [90] C. Habchi, T. Lemenand, D. Della Valle, H. Peerhossaini, Turbulence statistics downstream of a vorticity generator at low Reynolds numbers, *Phys. Fluids* 28 (10) (2016) 105106.
- [91] B. Herzhaft, É. Guazzelli, Experimental study of the sedimentation of dilute and semi-dilute suspensions of fibres, *J. Fluid Mech.* 384 (1999) 133–158.
- [92] V. Kantsler, R.E. Goldstein, Fluctuations, dynamics, and the stretch-coil transition of single actin filaments in extensional flows, *Phys. Rev. Lett.* 108 (3) (2012) 038103.
- [93] Y.-N. Young, M.J. Shelley, Stretch-coil transition and transport of fibers in cellular flows, *Phys. Rev. Lett.* 99 (5) (2007) 058303.
- [94] M. Sun, Insect flight dynamics: stability and control, *Rev. Mod. Phys.* 86 (2) (2014) 615.
- [95] Z.J. Wang, Dissecting insect flight, *Annu. Rev. Fluid Mech.* 37 (2005) 183–210.
- [96] C. Peterson, J. Strickland, H. Higuchi, The fluid dynamics of parachute inflation, *Annu. Rev. Fluid Mech.* 28 (1) (1996) 361–387.
- [97] K. Takizawa, D. Montes, M. Fritze, S. McIntyre, J. Boben, T.E. Tezduyar, Methods for fsi modeling of spacecraft parachute dynamics and cover separation, *Math. Models Methods Appl. Sci.* 23 (02) (2013) 307–338.
- [98] P. Vlasogiannis, G. Karagiannis, P. Argyropoulos, V. Bontozoglou, Air–water two-phase flow and heat transfer in a plate heat exchanger, *Int. J. Multiph. Flow* 28 (5) (2002) 757–772.
- [99] W. Qu, I. Mudawar, Flow boiling heat transfer in two-phase micro-channel heat sinks—I. Experimental investigation and assessment of correlation methods, *Int. J. Heat Mass Transf.* 46 (15) (2003) 2755–2771.
- [100] M. Ishii, T. Hibiki, *Thermo-Fluid Dynamics of Two-Phase Flow*, Springer Science & Business Media, 2010.
- [101] S.H. Davis, *Theory of Solidification*, Cambridge University Press, 2001.
- [102] R. Bonhomme, J. Magnaudet, F. Duval, B. Piar, Inertial dynamics of air bubbles crossing a horizontal fluid–fluid interface, *J. Fluid Mech.* 707 (2012) 405–443.
- [103] P.-G. De Gennes, F. Brochard-Wyart, D. Quéré, *Capillarity and Wetting Phenomena: Drops, Bubbles, Pearls, Waves*, Springer Science & Business Media, 2013.
- [104] W.-X. Huang, H.J. Sung, Three-dimensional simulation of a flapping flag in a uniform flow, *J. Fluid Mech.* 653 (2010) 301–336.
- [105] K. Shoele, R. Mittal, Energy harvesting by flow-induced flutter in a simple model of an inverted piezoelectric flag, *J. Fluid Mech.* 790 (2016) 582–606.
- [106] C.S. Peskin, B.F. Printz, Improved volume conservation in the computation of flows with immersed elastic boundaries, *J. Comput. Phys.* 105 (1) (1993) 33–46.
- [107] S. Xu, Z.J. Wang, An immersed interface method for simulating the interaction of a fluid with moving boundaries, *J. Comput. Phys.* 216 (2) (2006) 454–493.
- [108] S. Xu, Z.J. Wang, Systematic derivation of jump conditions for the immersed interface method in three-dimensional flow simulation, *SIAM J. Sci. Comput.* 27 (6) (2006) 1948–1980.
- [109] G. Li, Y. Lian, Y. Guo, M. Jemison, M. Sussman, T. Helms, M. Arienti, Incompressible multiphase flow and encapsulation simulations using the moment-of-fluid method, *Int. J. Numer. Methods Fluids* 79 (9) (2015) 456–490.
- [110] M. Vahab, K. Shoele, M.Y. Hussaini, M. Sussman, A Continuous Moment-of-Fluid Method with Reconstructed Distance Function for Simulating Multiphase Flows, 2020, unpublished.
- [111] G. Weymouth, D.K.-P. Yue, Conservative volume-of-fluid method for free-surface simulations on Cartesian-grids, *J. Comput. Phys.* 229 (8) (2010) 2853–2865.
- [112] P. Stephan, C. Busse, Analysis of the heat transfer coefficient of grooved heat pipe evaporator walls, *Int. J. Heat Mass Transf.* 35 (2) (1992) 383–391.
- [113] V.K. Dhir, Numerical simulations of pool-boiling heat transfer, *AIChE J.* 47 (4) (2001) 813–834.
- [114] P. Stephan, J. Hammer, A new model for nucleate boiling heat transfer [Neues modell für den wärmeübergang beim blasensieden], *Heat Mass Transf.* 30 (2) (1994) 119–125.
- [115] P. Stewart, N. Lay, M. Sussman, M. Ohta, An improved sharp interface method for viscoelastic and viscous two-phase flows, *J. Sci. Comput.* 35 (1) (2008) 43–61.
- [116] M.M. Francois, S.J. Cummins, E.D. Dendy, D.B. Kothe, J.M. Sicilian, M.W. Williams, A balanced-force algorithm for continuous and sharp interfacial surface tension models within a volume tracking framework, *J. Comput. Phys.* 213 (1) (2006) 141–173.
- [117] M. Arienti, M. Sussman, An embedded level set method for sharp-interface multiphase simulations of diesel injectors, *Int. J. Multiph. Flow* 59 (2014) 1–14.
- [118] M. Sussman, M. Ohta, A stable and efficient method for treating surface tension in incompressible two-phase flow, *SIAM J. Sci. Comput.* 31 (4) (2009) 2447–2471.
- [119] G. Li, Y. Lian, Y. Guo, M. Jemison, M. Sussman, T. Helms, M. Arienti, Incompressible multiphase flow and encapsulation simulations using the moment-of-fluid method, *Int. J. Numer. Methods Fluids* 79 (9) (2015) 456–490.
- [120] I. Lee, H. Choi, A discrete-forcing immersed boundary method for the fluid–structure interaction of an elastic slender body, *J. Comput. Phys.* 280 (2015) 529–546.
- [121] A. Goza, T. Colonius, A strongly-coupled immersed-boundary formulation for thin elastic structures, *J. Comput. Phys.* 336 (2017) 401–411.
- [122] A. Jacobi, R. Shah, Heat transfer surface enhancement through the use of longitudinal vortices: a review of recent progress, *Exp. Therm. Fluid Sci.* 11 (3) (1995) 295–309.
- [123] B. Lotfi, M. Zeng, B. Sundén, Q. Wang, 3d numerical investigation of flow and heat transfer characteristics in smooth wavy fin-and-elliptical tube heat exchangers using new type vortex generators, *Energy* 73 (2014) 233–257.
- [124] W. Kays, M. Crawford, *Convective Heat and Mass Transfer*, McGraw Hill, New York, 1993.